The Pennsylvania State University

The Graduate School

College of Earth and Mineral Sciences

TIME-LAPSE IMPEDANCE INVERSION AT POPEYE FIELD, OFFSHORE GULF OF MEXICO

A Thesis in
Geosciences

by

Tin-Wai Lee

Submitted in Partial Fulfillment
of the Requirements
for the Degree of

Master of Science

December 2003

The thesis of Tin-Wai Lee was reviewed and approved* by the following:

Peter B. Flemings
Associate Professor of Geosciences
Thesis Advisor

Charles J. Ammon
Associate Professor of Geosciences

Sridhar Anandakrishnan
Associate Professor of Geosciences

Peter Deines
Professor of Geosciences
Associate Head for Graduate Programs and Research

*Signatures on file in the Graduate School.

I grant The Pennsylvania State University the non-exclusive right to use this work for the University's own purposes and to make single copies of the work available to the public on a not-for-profit basis if copies are not otherwise available.

_____

Tin-Wai Lee

ABSTRACT

Time-lapse (4D) inversion is a stand-alone method that does not require prior time-lapse seismic processing because amplitude and phase differences in the input seismic data are accounted for within the inversion procedure itself. After 4.5 years of gas production, the impedance of the G-sand in the RM reservoir compartment increases by 6% and the gas-water contact is interpreted to move about 800 m westward and 90 m vertically upwards. These results are comparable to Gassmann fluid substitution forward modeling (8 % increase) and a volumetric drainage model (700 m westward). This time-lapse inversion method relies on wavelet estimation techniques to derive appropriate wavelets for the inversions.

TABLE OF CONTENTS

LIST OF FIGURES

LIST OF TABLES

PREFACE

This thesis is composed of a preface, a main body, an appendix, and an insert in the back pocket. The preface (viii-ix) explains the content and order of the constituents of the thesis and distinguishes between team and my individual contributions.

The main body of this thesis (1-42) results from my individual research performed as part of the Petroleum Geosystems Initiative, which is a multi-disciplinary M.S. program. This program consists of four graduate students (Eric Kuhl, Tin-Wai Lee, Benjamin Seldon, and Beth Yuvancic Strickland) who have approached the analysis of Popeye Field in the Gulf of Mexico from the disciplines of geology, geophysics, petrophysics, and petroleum engineering. The body of the thesis presents my work comparing two methods of time-lapse acoustic impedance inversion of post-stack seismic data. The two methods have been applied to determine the magnitude and location of impedance changes at Popeye due to 4.5 years of gas production. These time-lapse changes are represented in the same calibrated unit as Gassmann fluid substitution modeling, which models velocity as a function of rock and fluid properties.

Appendix A (43-61) is the joint collaboration with Beth Yuvancic-Strickland using Gassmann fluid substitution modeling at four well locations at Popeye field, as such modeling is relevant to the separate research of both individuals. This appendix will also appear as an insert in the Master's thesis of Beth Yuvancic Strickland.

The insert in the back pocket is a reprint of the paper, 'Integration of Geologic Model and Reservoir Simulation, Popeye Field, Green Canyon 116.' This paper is the result of the collaboration of the four members of the Petroleum Geosystems Initiative.

This work was presented in poster format by Kuhl and in presentation format by Strickland at the Gulf Coast Association of Geological Societies (GCAGS) 53rd Annual Convention in October 2003 and published in the transactions of the convention. Since the content of this paper contains background information relevant to this thesis and since the paper has four co-authors, the reprint is included in the back cover of this thesis.

The following is a reproduction of the email from Regina Vasilatos-Younken (Senior Associate Dean of the Graduate School) to Peter B. Flemings (thesis advisor) regarding the inclusion of this co-authored paper:

From: Regina Vasilatos-Younken <rxv@psu.edu>
To: flemings@geosc.psu.edu
cc: pml3@psu.edu
Subject: Re: Email From Flemings in Preparation for 11:15 tel. call today.

Peter - As we discussed today, a mutually agreeable solution to your request is to have the students who are participating in the GeoSystems Initiative position their individual research chapters in the body of the thesis (e.g., following an appropriate literature review and introduction), which would then be followed by an introduction to the collaborative project and paper product, and referring the reader to the paper (to be formatted as a journal article/preprint) contained in a pocket on the back cover of the hard bound thesis. This paper would list all four students as co-authors. When the students submit their respective theses to the thesis office, they need to submit the appropriate number of copies of this paper for each copy of the thesis to be bound, and indicate that it is to go in a pocket on the back cover. There is no extra charge by the University Libraries to the individual student for these special accommodations in the binding process for the "official copy" that will be archived in the Library.

If you have any questions regarding this approach, please don't hesitate to contact me. Congratulations on what sounds like an excellent experience for the students and one which prepares them in a meaningful way for working collaboratively in the "real world" of research.

Jean

Regina Vasilatos-Younken, Ph.D.

Professor of Endocrine Physiology & Nutrition, and
Senior Associate Dean of the Graduate School
114 Kern Graduate Building
The Pennsylvania State University
University Park, PA 16802
Tele: (814) 865-2516
Fax: (814) 863-4627
E-mail: rxv@psu.edu

ACKNOWLEDGEMENTS

The Shell Foundation, Shell Exploration and Production Company (SEPCo), Chevron-Texaco, Amerada Hess, Anandarko, Landmark Graphics, and Pennsylvania State University all support the Geosystems Initiative, of which this work is a part. SEPCo, Western-Geco, and CGG provided the data. The inversions presented in this thesis were performed using Jason Geoscience Workbench.

I would like to thank my advisor Peter B. Flemings, for giving me the freedom to pursue this study and for his confidence in my abilities. Peter has never given me the answer on a platter, instead he has instilled in me his of philosophy of "learning by doing." Peter also provided his unique perspective to Popeye. I also thank my committee members, Chuck Ammon and Sridhar Anandakrishnan for their insight and their useful courses. I also appreciate the input and advice of Turgay Ertekin. Heather Johnson, Rachel Altemus, Stefanie McCormick, and Tom Canich made my time at Penn State as smooth as possible by keeping everything organized and running.

I want to thank Benjamin Seldon, Beth Strickland, and Eric Kuhl for…for…for…uhm… Honestly, I am grateful for their insight and collaboration on the analysis of Popeye, while maintaining a fun atmosphere throughout. Ben introduced me to the world of Chris Moyles, Judge Jules, and Dave Pearce. He also played the role of big brother by looking out for me, making sure I have a good time, and letting me tag along with his friends. Beth was my solace when the presence of the boys was overwhelming; she also gave me advice on all things practical and normal in the world, of which I have no knowledge. Eric was also a big brother who was always on my side

and had many helpful suggestions, especially after consuming copious amounts of caffeine. I also thank Paul Strickland for his unwavering willingness to help (particularly with my Aprilia), for his craziness, and for watching scary movies with me. Aaron Janssen, Brandon Dugan, and Joe Comisky provided much information even after leaving Penn State.

The Green Canyon Production and Surveillance Asset Team of SEPCo (Anne Burke, Scott Baker, Rob Sloan, Dick Eikmans, Jeff Weiland, Alper Fer, Rose Lipton, Barbara Tisdale, and Malou Guerrero-Lee) made my internships very rewarding. They provided insight on Popeye and on the workings of the petroleum industry, and always had open doors. I am especially indebted to Anne Burke and Scott Baker. My second summer at Shell would not have been possible without Anne; she authorized and offered me the internship, funded me, provided an office with two new computers, and helped me find a place to live. Above all, she is an inspiration as a successful, intelligent, eloquent, and caring individual. Scott Baker helped develop the hypothesis for this study and provided insight and support. His dry sense of humor and web-surfing abilities enriched the experience. I also thank Selma Hawk for finding and loading my data, and T. Charles Jones for his processed data and insight.

Finally, I am grateful to my family for allowing the youngest child and only daughter to leave home to pursue graduate studies in geosciences. I know I am hard to predict and I always do the unexpected.

INTRODUCTION

Time-lapse acoustic impedance inversion combines time-lapse seismic analysis (e.g. Swanston et al., 2003) with acoustic impedance inversion (e.g. Madiba and McMechan, 2003; Pendrel and van Riel, 1997; Gluck et al., 2000) to determine the magnitude and location of impedance changes associated with production. Time-lapse seismic analysis is the comparison of multiple 3D seismic surveys that image the same location at different times (baseline initial time and monitor new time). Acoustic impedance inversion converts post-stack seismic data from amplitudes to acoustic impedance.

Inversion of seismic data into impedance allows quantitative interpretation (Latimer et al., 2000). Direct impedance comparisons can be made between different locations or between the same location at different times. It is an absolute layer property instead of a relative interface property and can image gradational changes. Impedance can be correlated to porosity, pore-fluid type, and lithology. False stratigraphic geometries caused by tuning and interference are reduced because inversion accounts for the wavelet sidelobe effects (Latimer et al., 2000). Impedance is a broadband dataset because it merges the bandwidth of seismic data and the low-frequency bandwidth of well log data. Random noise is attenuated in the inversion, resulting in increased signal-to-noise ratio (Pendrel and van Riel, 1997).

Time-lapse impedance inversion seeks to provide a quantitative link between amplitude change and the physical changes that have occurred in the reservoir due to production. There are several approaches to solving this inverse problem. Tennebo et al. (1998) proposed a sequential, model-based time-lapse inversion workflow in which the

geostatistical kriging of well logs was the *a priori* model for the baseline inversion, the result of which was the *a priori* model for the monitor inversion. Both inversions were performed with the Best Feasible Approximation, which seeks a solution that is within the intersection of all constraint sets and is as close to the *a priori* model as possible (Malinverno, 1995). Gluck et al. (2000) formulated three different objective functions; one for the inversion of the base survey, one for the sequential inversion of the monitor survey, and one for the simultaneous differential inversion of the monitor survey. They used stratigraphic inversion (Gluck et al., 1997) and proposed that time-lapse inversion should account for the relationships between model parameters of the base and monitor surveys. Abubakar et al. (2001) created synthetic baseline and monitor data sets and compared two inversion strategies using the same nonlinear iterative procedure (Extended Contrast Source Inversion) based on conjugate gradient methods (van den Berg et al, 1999). They determined that inverting the base and monitor datasets separately and then subtracting them yielded better results than inverting the seismic difference. Mesdag et al. (2003) performed joint simultaneous amplitude-vs.-offset (AVO) inversion on three partial angle stacks. They simultaneously inverted baseline and monitor partial stacks, then simultaneously re-inverted both datasets with the previous results as the *a priori* models, with tight constraints outside the reservoir interval. This workflow and the incorporation of both acoustic and shear impedance inversion allowed them to image fluid movement, as well as improve discrimination of oil sands and coals, which have similar seismic signatures and acoustic impedance.

These studies largely focused on the time-lapse inversion techniques (i.e. the inversion algorithms, *a priori* models, objective functions, and parameterizations of the

solution space) and did not discuss the impact of pre-inversion seismic processing on the inversion result. Pre-processing was assumed to be necessary and only mentioned for special cases such as for land seismic data to account for near-surface phenomena (Gluck et al., 2000) and for combined time-lapse and AVO purposes (Mesdag et al., 2003).

This study addresses the question of whether seismic data sets should be normalized prior to time-lapse inversion. We use two methods of time-lapse inversion to examine impedance changes due to 4 1/2 years of gas production from the G-sand in the RM reservoir of Popeye Field in Green Canyon Block 116, Gulf of Mexico (Figure 1). In one method, we first normalize the base and monitor data sets before we invert them with the same wavelet (Figure 2a). In the second method we directly invert the non-processed base and monitor data sets using wavelets derived from each survey to compensate for their differences (Figure 2b). We then compare the time-lapse impedance results of these two methods.

BACKGROUND

The Popeye Field

The Popeye Field is a subsea development located in Green Canyon Blocks 72, 73, 116, and 117 in the offshore Gulf of Mexico (Figure 1a). From January 1996 to the present, the Popeye field has been producing gas and condensate from the late-Pliocene turbidite G-sand at 3500 m depth in 600 m of water. Production from the four G-sand reservoir compartments (RN and RM in the west, RA and RB in the northeast) is tied back to the Cougar platform in South Timbalier Block 300, 39 km to the north.

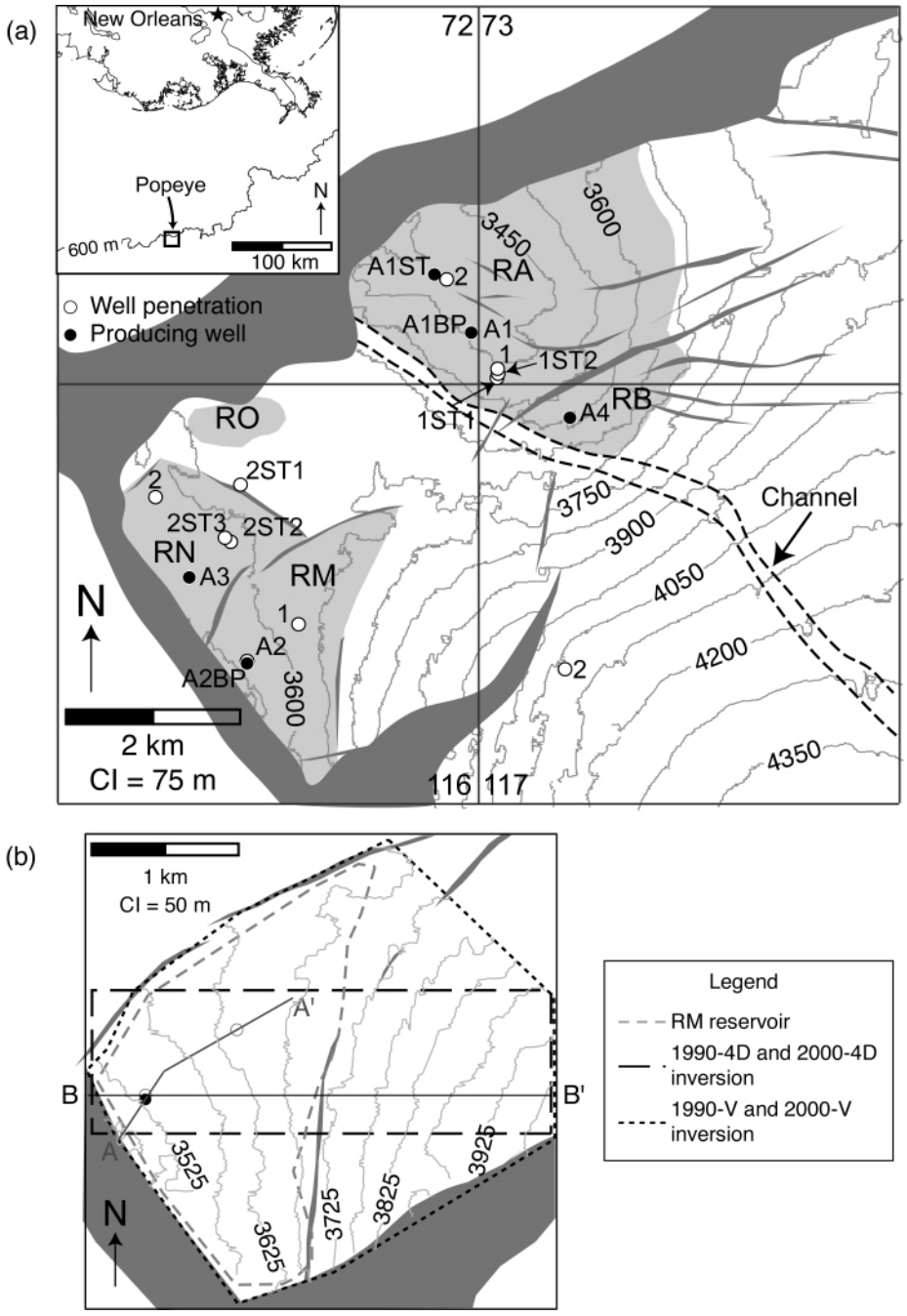

Fig. 1: (a) The Popeye field is located 230 km south of New Orleans in 600 m of water. Structure map of vertical subsea depth (TVDSS) in meters to the top of the G-sand with faults that intersect the G-sand in dark grey. The five reservoir compartments (light grey) are delineated by faults, an impermeable channel, and GWCs. (b) The lateral data coverage of the data inverted in the two methods in relation to the well penetrations and RM reservoir area. Line A-A' passes through the G-sand penetration of both wells and corresponds to the cross-section in Figure 6. Line B-B' passes through well A2 and corresponds to frequency spectrums in Figure 7 and cross-sections in Figures 9 and 10.

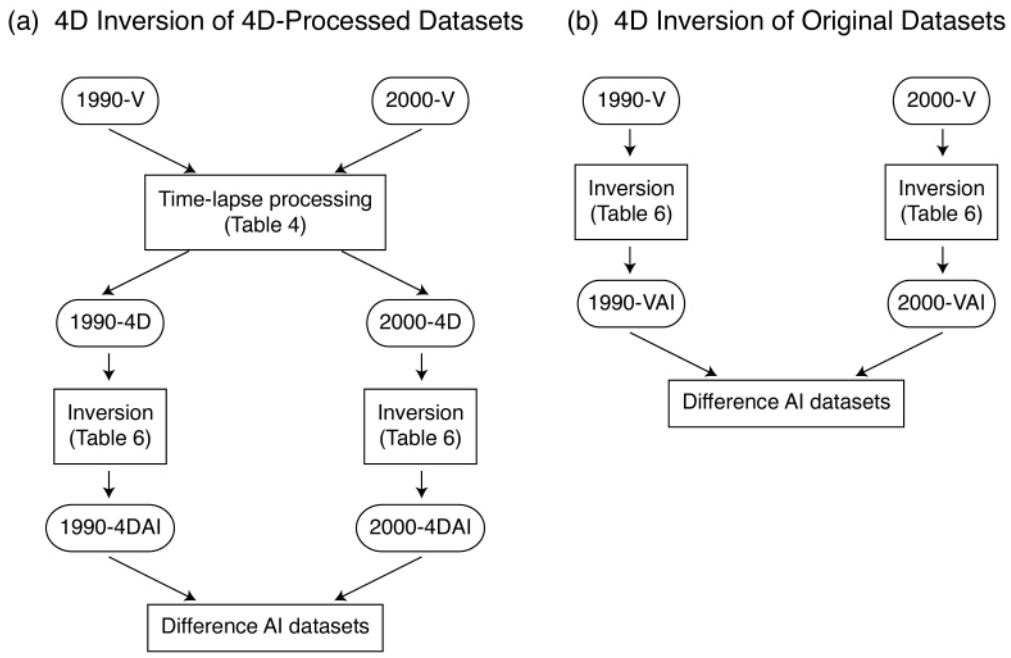

Fig. 2: Flowcharts of two methods of time-lapse inversion. In the first method (a), time-lapse seismic processing is followed by inversion with the same wavelet in both inversions. In the second method (b), the original, non-normalized data sets are inverted with separate wavelets for each inversion.

The field is on the southern downthrown side of a regional growth fault and the RM and RN compartments are bounded on the west by a normal fault that dips to the southwest (Figure 1b) . Smaller faults and a channel compartmentalize the G-sand into the four reservoir compartments (Yuvancic-Strickland et al., 2003). The RM compartment is the focus of this study because it had the greatest volume of gas production (125 billion cubic feet (BCF) between January 1996 to April 2002) (Figure 1c).

The laminated facies (G_L) and the underlying massive facies (G_M) comprise the G-sand, which averages 23 m in gross thickness at well penetrations (Figure 3). The G_L is a fine-grained, high porosity sandstone that is interbedded with silty shale. The G_M is a very fine-grained, clean sandstone with no internal structure and moderate sorting.

3D Seismic Surveys

A survey acquired in 1990 (1990-V) is used to image Popeye prior to the onset of production in January 1996 (Table 2). A 2000 survey (2000-V) is used to monitor the field after 4.5 years of gas production (Table 2). Both data sets were acquired in an east-west direction (90°); however, they have significant differences in other acquisition parameters and processing (Tables 3, 4).

We time-lapse invert these data with two methods (Figure 2). In one method, we invert the 1990-V and 2000-V post-stack surveys with no processing prior to inversion. In the second approach, we reprocess 2000-V and 1990-V to minimize their differences prior to inversion (Table 5). In both methods, the 2000-V data were regridded to the grid system of 1990-V.

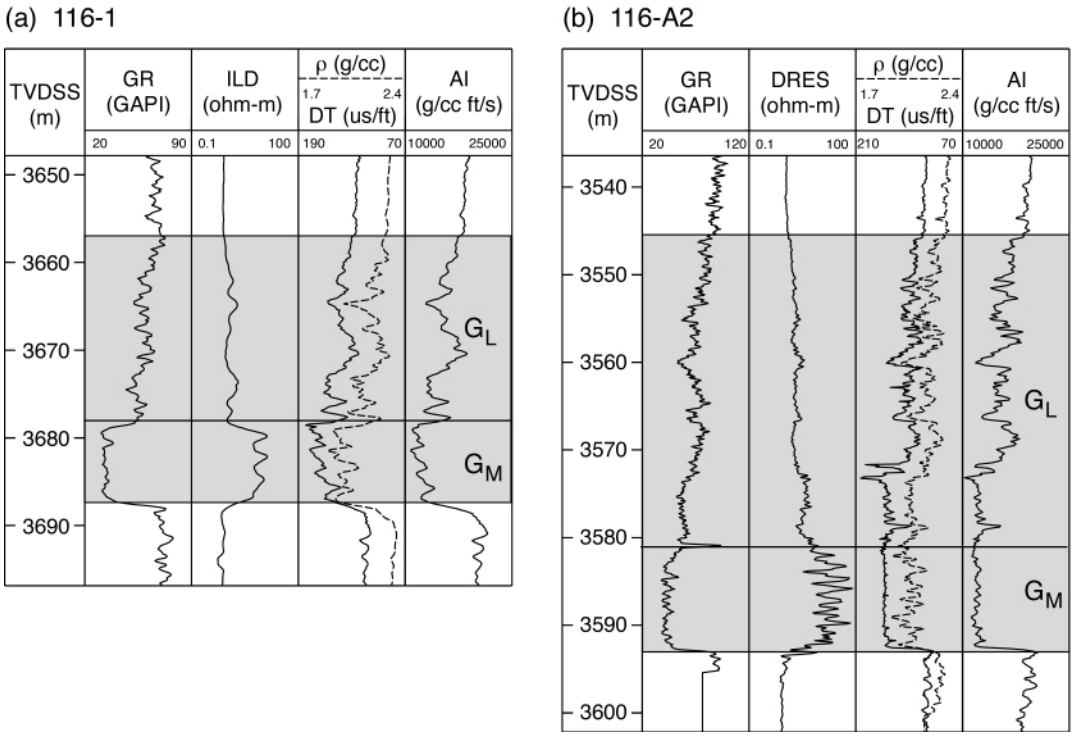

Fig. 3: Pre-production wireline log response of the G-sand at (a) well 1 and (b) well A2 showing gamma-ray (GR), resistivity (ILD and DRES), sonic (DT), and density (ρ) logs. Acoustic impedance (AI) is computed from the sonic and density logs. These logs show a ramped signature with increasing depth in the G_L, which can be interpreted as a combination of increasing porosity, bed thickness, and/or sand content.

Inversion with Preprocessing

Shell International Exploration and Production (SIEP) performed the reprocessing of 1990-V and 2000-V (Table 5). Due to time and cost constraints, only the un-migrated data that fell within the central portion of the RM reservoir were used (Figure 1c) and the data were decimated to every other east-west inline. Both data sets were limited to identical offset ranges and channel gains were applied. Then the monitor data were regridded to the base grid system. The same gain function was applied to and multiples were removed from both datasets. Each dataset was depulsed to zero-phase. Static corrections and dip move-out corrections were made to both datasets. To increase signal-to-noise ratio, a noise suppression filter was applied to both data sets. Pre-stack in-line migration was performed in a similar manner to both data sets.

A global match filter was applied to the monitor data to match the base data. The monitor data set was shifted in time to align with the base data set. A filter was applied to the monitor data to match the signal spectra of the base data, followed by a filter to match the phase. A trace-by-trace filter with moving overlapping windows was applied to both data sets. The same time-varying gain function and bandpass filter were performed on both data sets. The reprocessed 1990-V and 2000-V are hence the 1990-4D and 2000-4D (Table 2).

PROCEDURE

Inversion Workflow Overview

The inversion procedure of Pendrel and van Riel (1997) is performed to the four data sets (Table 6). A well-to-seismic tie and wavelet estimation are performed between

each of the two wells with each of the four data sets. Then a multi-well wavelet, which honors data at both wells, is estimated for each data set. Next we create a gridded impedance volume to provide a low-frequency trend that defines the constraints and is the *a priori* model for the inversion. Finally, the multi-well wavelet and Earth Model are used in a constrained sparse-spike inversion algorithm (Pendrel and van Riel, 1997) to invert each data set.

Wavelet Estimation

Kojo et al. (1990) and Dennis et al. (2000) demonstrated the importance of having an appropriate wavelet to calibrate the inversion of seismic data. We illustrate the well-to-seismic tie and wavelet estimation between well 1 and 1990-V (Figure 4); the same approach is used to derive wavelets between the other wells and data sets. Eight CDP locations are chosen along the well path around the G-sand (Figure 5B). The time window over which the wavelet is derived must contain well impedance, be located around the region of interest (G-sand), and be long enough so that there is enough data for a confident estimation of the wavelet but short enough to ensure that the signal is stationary (Pendrel and van Riel, 1997). At well 1, this window is between 3500 and 4340 ms (Figure 4). The wavelet length (194 ms or 41 samples) must be long enough so that the energy at the ends tapers smoothly to zero to avoid convolution artifacts, but short enough that it only includes the first sidelobe (Pendrel and van Riel, 1997).

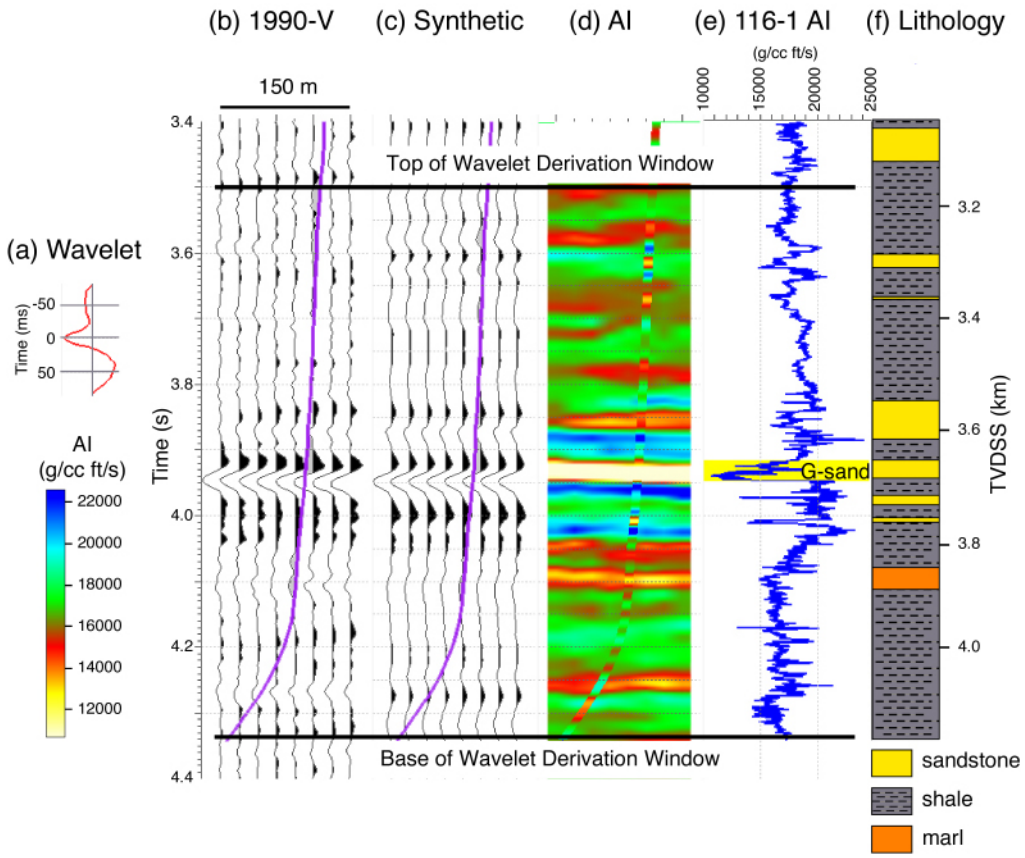

Fig. 4: Final well-to-seismic tie between well 1 and 1990-V. The linear vertical scale is time on the left; a nonlinear TVDSS scale is on the right. The wavelet (a) matches the eight observed 1990-V traces (b) with eight synthetic traces (c) derived from eight inverted impedance traces (d) and impedance at the well. A lithology log (f) is provided to correlate to the impedance log.

A two-step process is used to estimate the single-well wavelet (Figure 4a). In the first pass, the wavelet is estimated by computing a filter that minimizes in a least-squares sense, the difference between the eight observed seismograms (Figure 4b) and the single synthetic seismogram (e.g. White, 1980). The single synthetic trace is created by the convolution of the wavelet with the reflectivity series derived from the impedance at the well (Figure 4e). The phase of the wavelet, which can vary with frequency, is determined from the inverse of this filter (Pendrel and van Riel, 2000). We edit the time-depth relationship at the well so that the estimated wavelet is close to zero-phase.

In the second step, the eight observed seismograms (Figure 4b) are inverted to produce eight impedance traces (Figure 4d). The previous wavelet is updated until it minimizes the difference between the eight observed (Figure 4b) and eight modeled (Figure 4c) seismograms (White, 1980). These eight synthetic seismograms result from the convolution of the wavelet (Figure 4a) with eight reflectivity series derived from the eight impedance traces.

This procedure is repeated for well A2 with 1990-V; then a multi-well wavelet is estimated for use in the inversion of 1990-V. The multi-well wavelet minimizes the difference between the 16 observed and the 16 synthetic seismograms. It is not the average of the well 1 wavelet and the well A2 wavelet.

The wavelets of 1990-4D and 2000-4D are similar in peak amplitude, shape, phase, and frequency (Figure 5a, b). Similarity of wavelets between the two data sets indicates that the time-lapse processing achieved similarity in the scale, phase, and frequency content of the seismic data. The wavelet used in the inversion of 1990-4D and 2000-4D is the average of the multi-well wavelets of two data sets (Figure 5c).

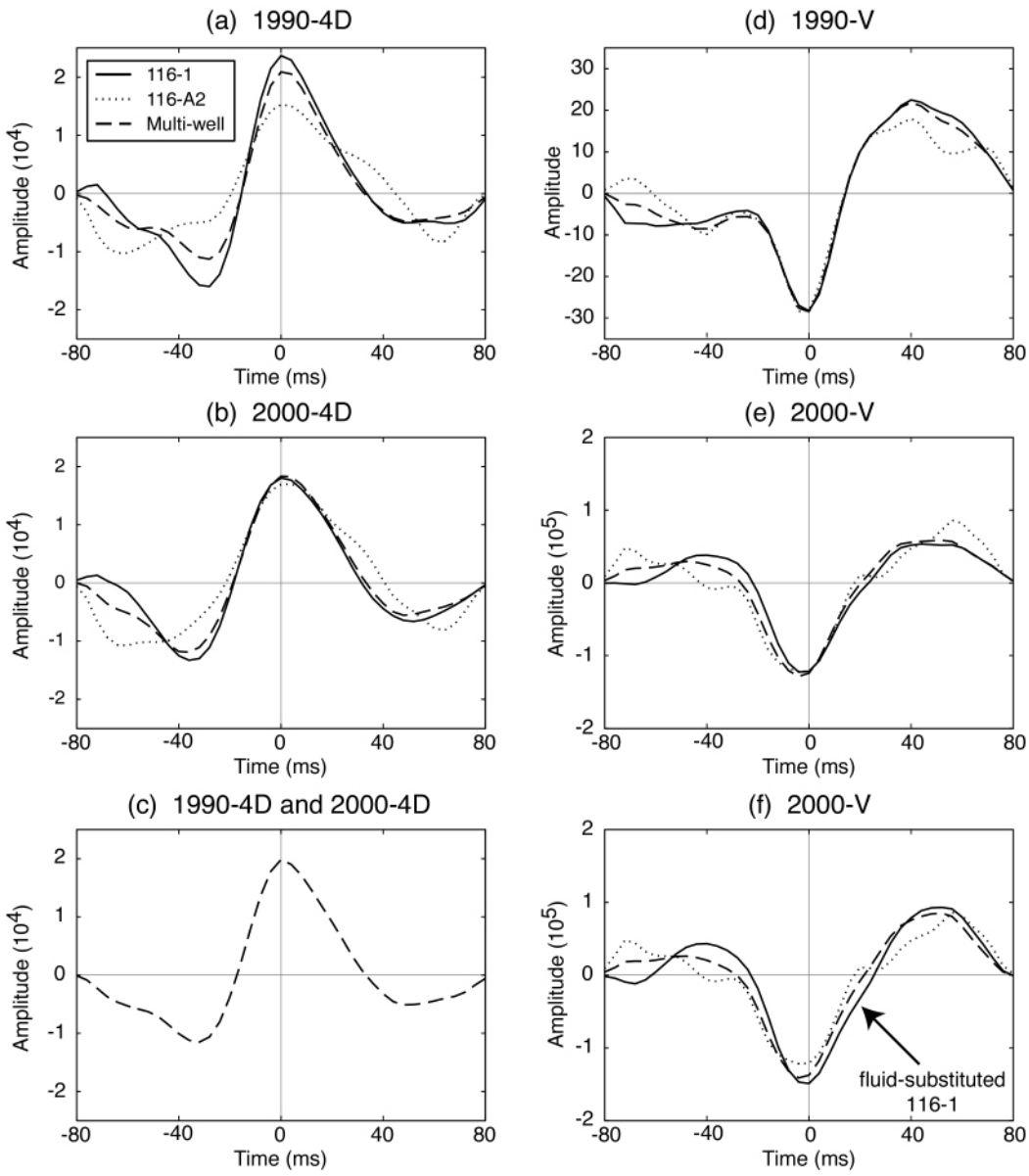

Fig. 5: Estimated single-well and multi-well wavelets for each data set. The wavelets from 1990-4D (a) and 2000-4D(b) are similar; the average (c) of the multi-well wavelet from 1990-4D and 2000-4D is used to invert both 1990-4D and 2000-4D. The 1990-V wavelets (d) have a small negative left lobe and a large positive right lobe. The 2000-V wavelets (e) have positive left and right lobes that are similar in magnitude. The 2000-V wavelets (f) in which well 1 is fluid substituted (well A2 remains the same) show that fluid substitution scales the wavelet so that the amplitudes are greater than without fluid substitution.

The wavelets of 1990-V and 2000-V are different in scale and shape (Figure 5d-f) because the 1990-V and 2000-V have not been normalized to each other. The 1990-V wavelets have a small negative left lobe and a large positive right lobe (Figure 5d). In contrast, the 2000-V wavelets have positive left and right lobes, with the right lobe slightly larger than the left (Figure 5e, f).

Fluid substitution is performed at well 1, where saturation changed in the time interval between the collection of the log and seismic data, in order to estimate a wavelet that is appropriately scaled. Since the logs at both wells were acquired before production, no fluid substitution is performed to estimate wavelets for the pre-production 1990-4D and 1990-V. The logs are not fluid substituted at well A2 because reservoir simulations and production history indicate there was little saturation changes at this location in mid-2000. We fluid substitute the logs at well 1 using pressure and saturations from the reservoir simulation results at well 1. See Appendix A for more information on fluid substitution modeling parameters.

The application of fluid substitution at well 1 results in a wavelet with greater amplitudes in the main and side lobes compared with the wavelet derived using the non-fluid substituted log (Figure 5e). We invert 2000-V twice; once with the multi-well wavelet that incorporates the fluid-substituted well 1 well and once without any fluid substitution to derive wavelets. The impedance results are similar and we ultimately present the results with fluid substitution. No fluid substitution is performed at well 1 for the estimation of the multi-well wavelet used to invert 2000-4D because we interpret that it would also have a small effect on the impedance results.

The *A Priori* Model

We reconstruct the low-frequency information that is missing from band-limited seismic data (Dennis et al., 2000; Ghosh, 2000; Pendrel and van Riel, 2000). First we interpolate and extrapolate impedance from the two wells in two-way time using the Natural Neighbor algorithm (Sakhnovich, 1997) to create an acoustic impedance volume with the same dimensions (Figure 1c), number of traces, and sample interval as the input seismic data (Figure 6). Horizons and faults interpreted from the seismic data are used to guide the interpolation so that it parallels strata (Table 7). Next we filter the volume to produce the low-frequency (0 - 6 Hz) trend, which corresponds to the missing bandwidth determined from spectral analysis of the seismic data (Figure 7).

This low-frequency trend serves two other purposes besides providing information that is below the bandwidth of the seismic data. The inversion algorithm uses it as the *a priori* model to help establish the starting-point in the search for a solution. Secondly, the inversion constraints are set by limiting the solution search to be within one standard deviation of the trend.

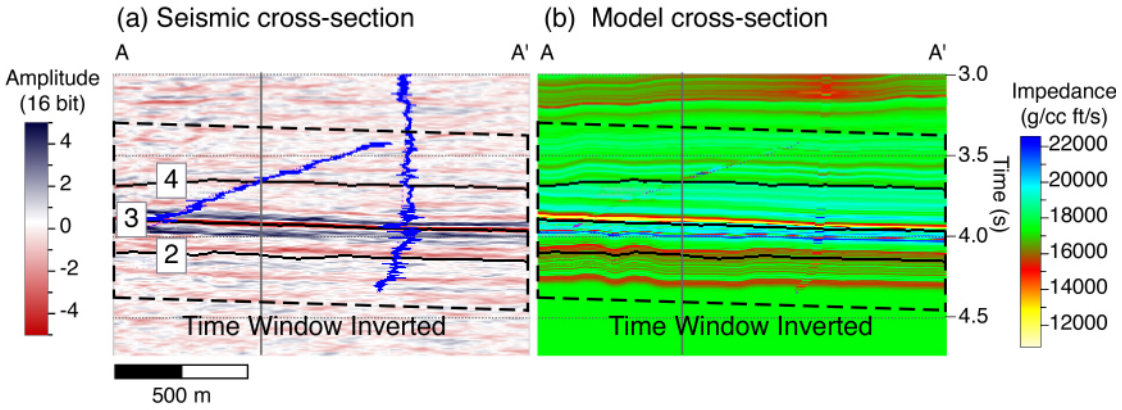

Fig. 6: (a) 1990-V cross-section A-A' (located on Figure 1b) through wells A2 and 1 with impedance at wells in blue. (b) Cross-section A-A' through the unfiltered interpolated impedance volume overlain by impedance at wells. Black Horizons interpreted from 1990-V (Table 7) guide the interpolation of the well impedances. The *a priori* model is the low frequency (0-6 Hz) portion that is used in the inversion of the one-second volume centered around the G-sand.

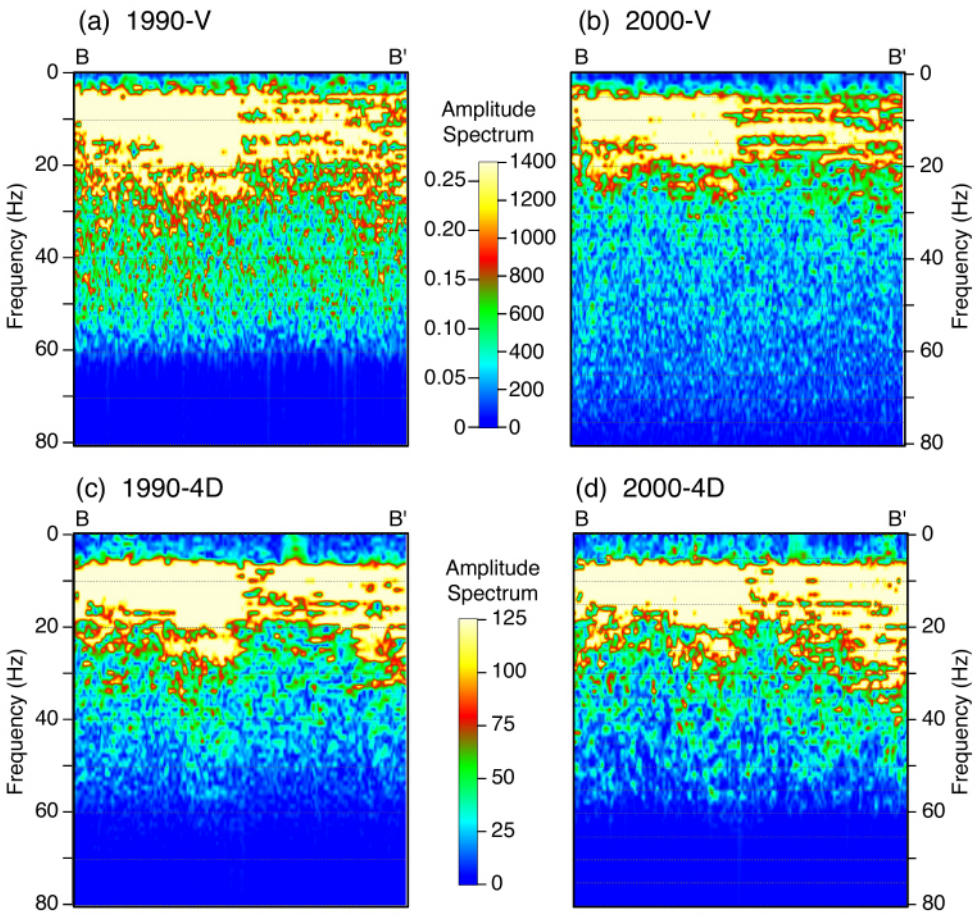

Fig. 7: Frequency spectrums of (a) 1990-V, (b) 2000-V, (c) 1990-4D, and (d) 2000-4D along line B-B' (location in Figure 1b). The normalized data are more band-limited; they are missing data from high and low frequencies present in the non-normalized data. The spectra of 1990-V and 2000-V are missing between 0-4 Hz, whereas the spectra of 1990-4D and 2000-4D are missing between 0-6 Hz. To be consistent, the *a priori* model has the same bandwidth (0-6 Hz) for the inversion of all four datasets.

Inversion

We invert a one-second volume centered around the G-sand. Each observed seismic trace (A_{obs}) is modeled as the convolution of the reflection coefficients (r_A) with the multi-well wavelet (w):

$$A_{obs} = r_A * w. \tag{1}$$

The first step is to invert for the reflection coefficients r_A (e.g. Debeye and van Riel, 1990). The r_A at each trace are integrated and merged with the *a priori* model for an estimate of impedance.

Constrained inversion for impedance is performed using this estimate as a starting point. Inversion is a trace-by-trace optimization problem that seeks the impedance trace that minimizes the vector norms (Eq. 2) of the objective function (Eq. 3). The Lp-norm of a vector x is

$$\|x\|_p = \left(\sum |x_i|^p\right)^{1/p}. \tag{2}$$

The inversion objective function at each trace is

$$F = \|r_z\|_{0.9} + \lambda \|A_{syn} - A_{obs}\|_2 + \|z_{trend,inv} - z_{trend,model}\|_1, \tag{3}$$

where F is the total misfit of the one-second inverted impedance trace, r_z is the reflectivity series, λ is a scaling factor, A_{syn} is the synthetic seismogram, A_{obs} is the observed seismogram, $z_{trend,inv}$ is the low-frequency trend of the inverted impedance trace, $z_{trend,model}$ is the low-frequcny *a priori* model. The reflectivity series r_z is defined by the inverted impedance trace z by

$$r_z = \frac{z_{i+1} - z_i}{z_{i+1} + z_i}. \tag{4}$$

The synthetic seismogram A_{syn} is the convolution of r_z with w. Since the objective function has terms for three different quantities, the norms are normalized by their standard deviations before they are summed into the total misfit.

The first term of the objective function is an L0.9-norm of the reflectivity series. Minimization of this term stabilizes the calculation and favors impedance traces that have simple reflectivity series (ie with sparse, large reflection coefficient spikes). We use an L0.9-norm (p = 0.9) because the distribution of reflection coefficients is generally non-Gaussian (Walden and Hosken, 1986); moreover, the presence of the gas-saturated G-sand in the one-second inversion volume results in outliers. We use an L0.9-norm (p = 0.9) rather than an L1-norm (p = 1) to favor the impedance traces that are simpler. Values of p less than 1 favor simpler solutions; values of p greater than 1 favor band-limited solutions.

The second term of the objective function is an L2-norm of the difference between synthetic and observed seismic traces (the seismic residual). We use an L2-norm (p = 2) because we expect the seismic residuals to have a Gaussian distribution. Minimization of this term favors impedance traces whose synthetic traces are most similar to the observed seismic traces.

The third term of the objective function is an L1-norm of impedance trend misfit, which is the difference between the low-frequency *a priori* model and the low-frequency inverted impedance trend. We use an L1-norm (p = 1) because we do not expect this difference to have a Gaussian distribution. Minimization of this term will stabilize the calculations and reduce non-uniqueness in the impedance solutions by not considering solutions that are geologically and geophysically unrealistic.

The first and second terms of the objective function cannot both be minimum simultaneously. Since the benefits of these two terms trade off, they are balanced with the scaling factor λ. A low λ results in an overly simple reflectivity series, a less detailed inverted impedance model, and synthetic traces that does not match the observed seismic trace (large seismic residuals). A high λ results in a detailed reflectivity series, a complicated inverted impedance model, false events being modeled, and synthetic traces that match observed seismic traces (including noise). We test a range of λ values to determine that a λ □□.12 yields seismic residuals that are mostly in the frequency spectrum of the noise of the input data.

RESULTS

Objective Function Results

The values of the three norms of the minimized objective function for each one-second trace of the final inversion solution of 1990-V are shown in Figure 8. The reflectivity norm ($||r||_{0.9}$) is highest in traces where the G-sand has highest amplitudes because the large RFCs that are required to model the G-sand where it is gas-saturated contribute greatly to the reflectivity norm of the one-second trace (Figure 8a).

The norm of seismic residuals ($||A_{syn} - A_{obs}||_2$) is consistent across the entire inverted area (Figure 8b). The λ of 12 results in differences between the input 1990-V and synthetic seismic traces that are within the level of noise in 1990-V, which is consistent across the area. Inversion attenuates noise by not matching the noise portion of the input seismic data.

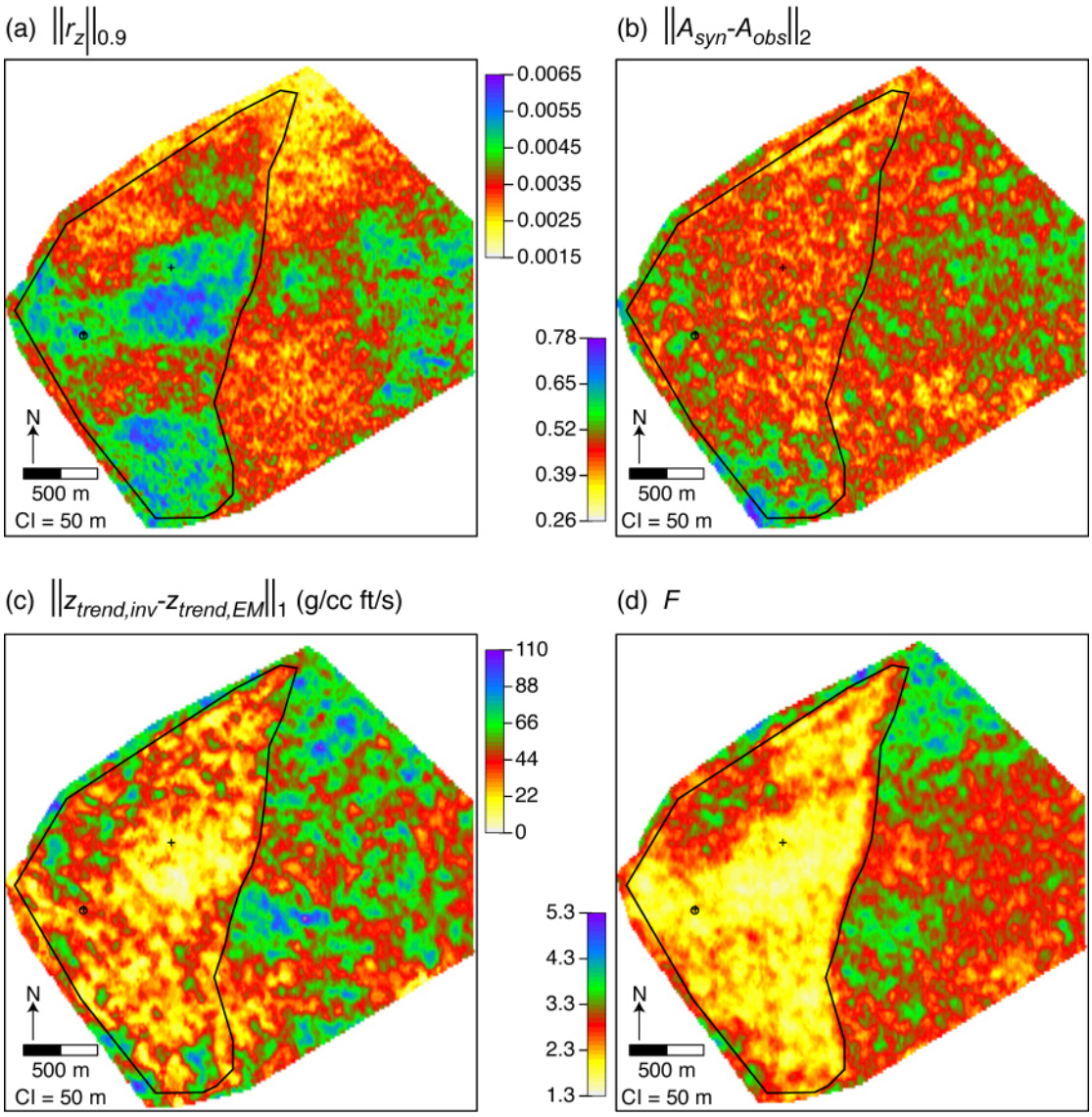

Fig. 8: Values of the three terms of the objective function and their normalized sum at each one-second impedance solution of the inversion of 1990-V (Eq. 2). (a) The L0.9-norm of reflectivity. (b) The L2-norm of seismic residuals. (c) The L1-norm of impedance trend misfit in g/cc ft/s. (d) The total normalized misfit.

The norm of low-frequency impedance trend misfit ($||z_{trend,inv} - z_{trend,model}||_1$) is lower for traces in the reservoir area than in the aquifer (Figure 8c); the misfit occurs mostly within the G-sand interval of the one-second inverted trace. This is expected because the *a priori* model is not valid within the G-sand interval in the aquifer region; we interpolate and extrapolate the impedance from the two wells in the gas-saturated reservoir area to populate the *a priori* model. As a result, the solution within the aquifer G-sand interval is far from the *a priori* model.

The total misfit (F), or sum of the three normalized norms, is lower for traces in the reservoir than the aquifer because of the large influence of the norm of the low-frequency impedance trend misfit (Figure 8d). The results of the inversion of 2000-V, 1990-4D, and 2000-4D exhibit similar patterns as 1990-V.

Impedance Results

The minimum impedance G-sand map from 1990-4DAI shows that the reservoir is low impedance and has a smooth pattern (Figure 9a). The minimum impedance G-sand map from 2000-4DAI shows that the reservoir experiences an overall increase in impedance and has a patchy pattern (Figure 9b). This impedance increase and pattern change from smooth to patchy in the reservoir is also observed in cross-sections (Figure 9c,d). Both maps show a similar, high impedance aquifer. The original gas-water contact is clearly imaged in both 1990-4DAI and 2000-4DAI.

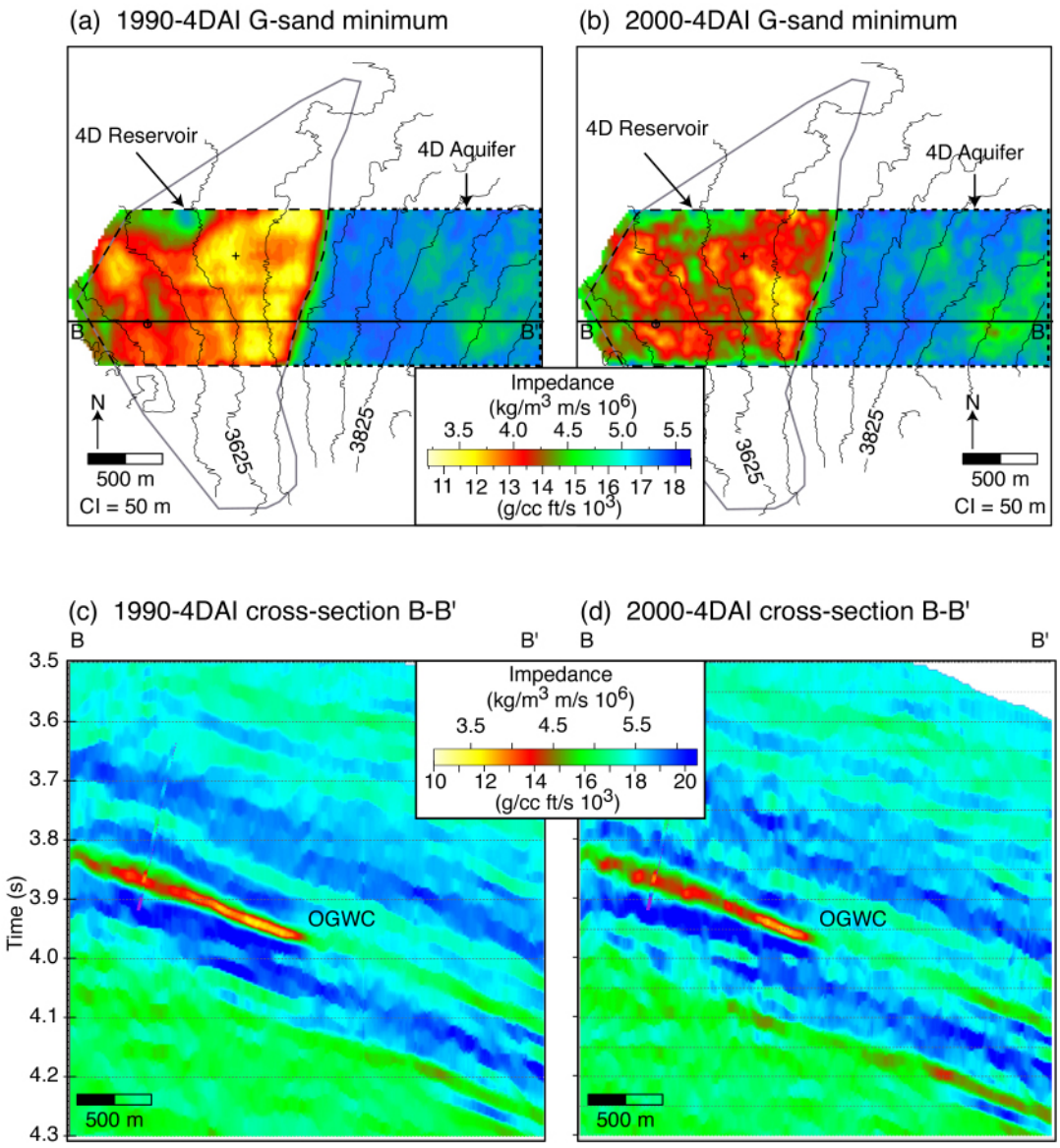

Fig. 9: Minimum impedance extraction maps of the G-sand from 1990-4DAI (a) and 2000-4DAI (b) with structure contours overlain. Cross-section B-B' through 1990-4DAI (c) and 2000-4DAI (d).

The inversions of 1990-V and 2000-V have similar first order results in map view and cross-section (Figure 10). The reservoir increases in impedance and becomes patchy while the aquifer remains high impedance and original contacts are clearly imaged. Also, in both methods the northwest region of the reservoir is relatively high impedance.

Closer comparison of the results of the two methods in the area of overlap shows that there are differences. The G-sand minimum impedance map of 1990-4DAI is smoother than 1990-VAI. The G-sand minimum impedance of 2000-4DAI is lower impedance than 2000-VAI and the low impedance patches are in different locations. In cross-section, the two high impedance layers below the G-sand are more distinct in 1990-VAI and 2000-VAI than in 1990-4DAI and 2000-4DAI.

Impedance Changes

The G-sand minimum impedance difference maps of both methods show that the aquifer experiences little to no change (Figure 11); the histograms of impedance change in the aquifer are narrow and centered near zero (Figure 12). Within the common aquifer, the two methods produce slightly different results (Table 8). The difference map of 1990-4DAI and 2000-4DAI has a median reduction of 113 g/cc ft/s (0.74%) whereas the difference map of 1990-VAI and 2000-VAI has a median increase of 114 g/cc ft/s (0.79%). Within the entire aquifer area in 1990-VAI - 2000-VAI, the results show that the aquifer has experienced a median increase of 22 g/cc ft/s (< 0.01%).

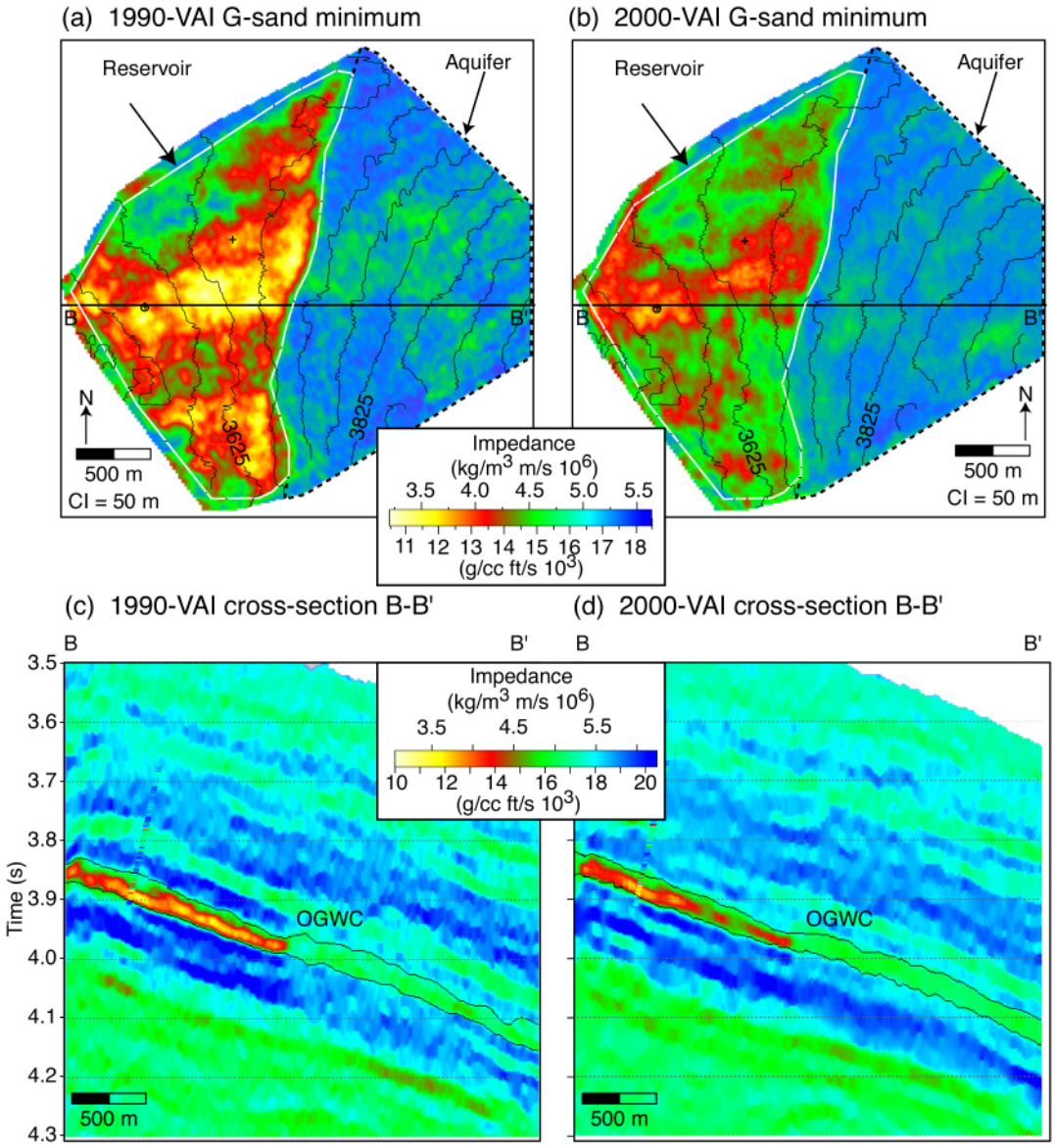

Fig. 10: Minimum impedance extraction maps of the G-sand from 1990-VAI (a) and 2000-VAI (b) with structure contours overlain. Cross-section B-B' through 1990-VAI (c) and 2000-VAI (d).

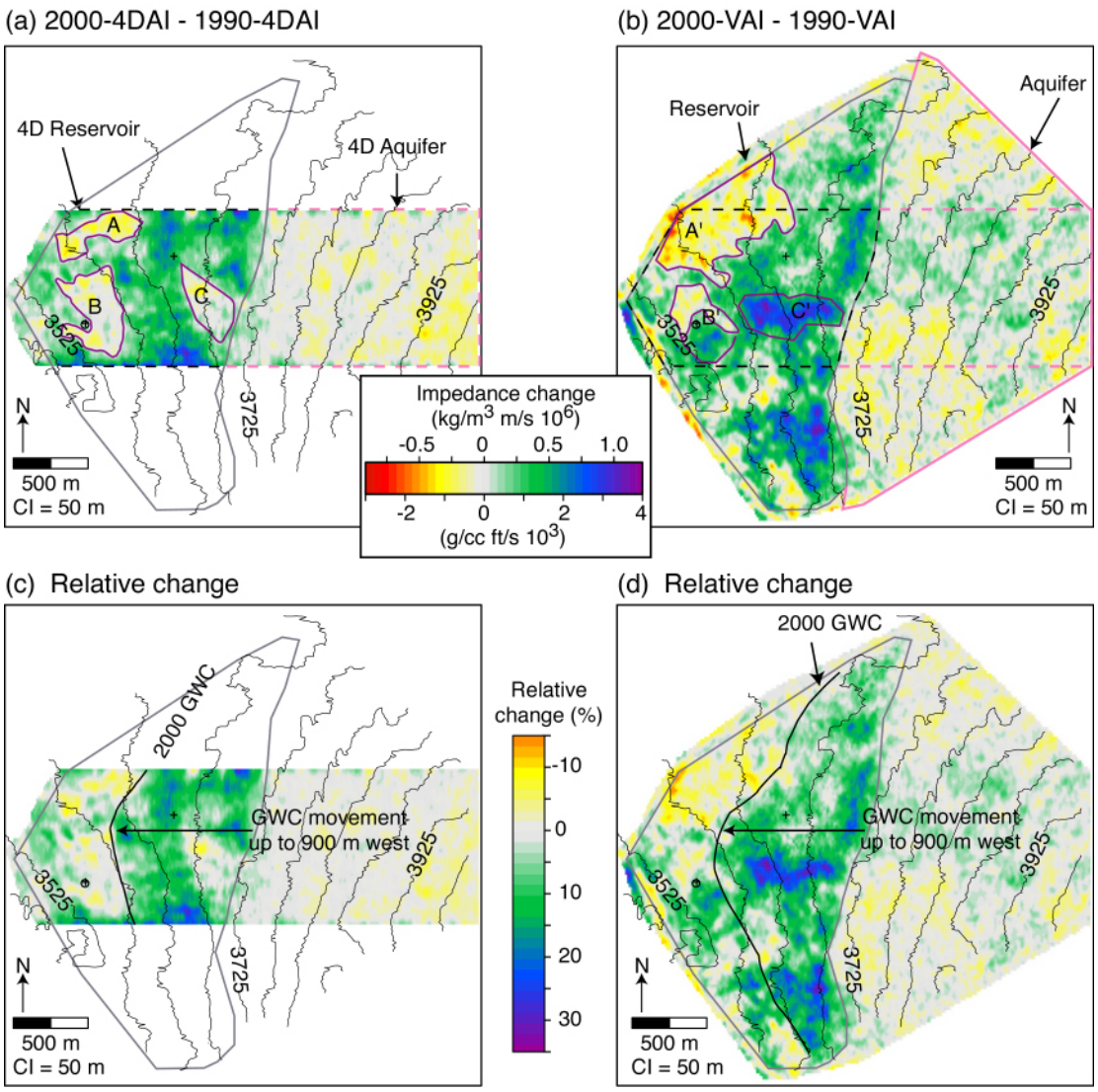

Fig. 11: G-sand minimum impedance difference map from (a) 4D inversion with 4D pre-processing and (b) from 4D inversion of original data. Positive change indicates an impedance increase and negative change indicates an impedance reduction. Purple polygons highlight areas discussed in the text. In both methods (c and d), the GWC moves westward by up to 900 m.

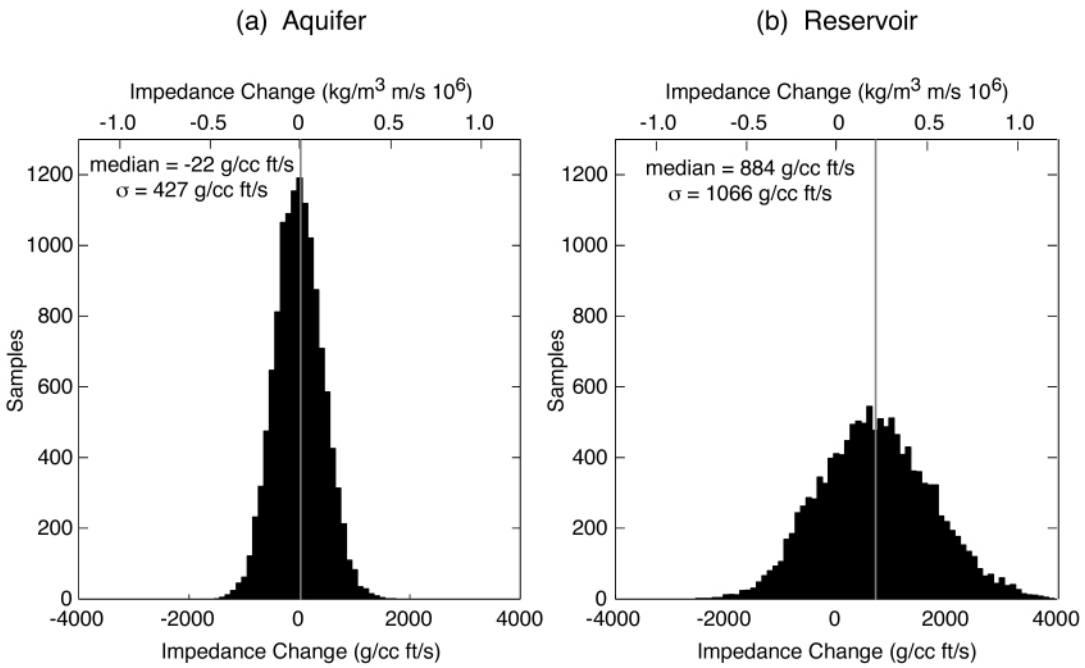

Fig. 12: (a) The histogram of impedance change in the aquifer (Figure 11b) showing a narrow distribution. (b) The histogram of impedance change in the reservoir (Figure 11b) showing a broad distribution.

The difference maps of both methods show that the reservoir increases in impedance, with a few localized areas of impedance reduction (Figure 11). The histograms of impedance change are broad and have a wide range (Figure 12). Within the common reservoir, the 4DAI difference map has a median impedance increase of 625 g/cc ft/s (5.80%); the VAI difference map has a median impedance increase of 884 g/cc ft/s (6.35%). The entire reservoir area increases in impedance by 690 g/cc ft/s (6.26%).

INTERPRETATION

Gas-water contact movement

Original GWCs are clearly imaged in base and monitor impedance maps of both methods. Mid-2000 GWCs are difficult to interpret on monitor maps alone; we interpret the new GWC on the difference maps where there are boundaries between impedance increase and no change (Figure 11c,b). In both methods, the GWC moves westward by up to 900 m and generally moves up structure by about 100 m.

These results are similar to the results of a simple drainage model (Figure 13), which predicts a horizontal GWC movement by 700 m and a vertical GWC movement of 90 m. In the simple drainage model (Figure 13), the G-Sand at the RM compartment is modeled to have a constant thickness, net-to-gross ratio, porosity, and dip. The surface volume of 104 BCF of gas that was produced by June 2000 is converted to the volume it formerly occupied in the reservoir and it is assumed that gas saturations change from 0.9 to 0.3 as water replaces gas.

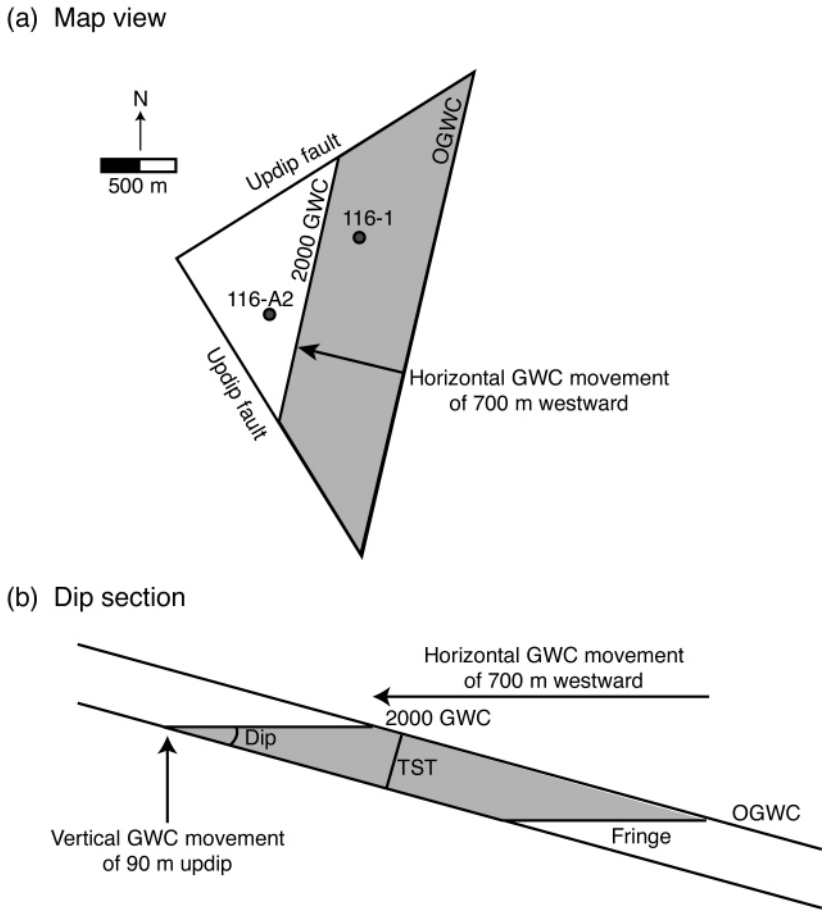

Fig. 13: Simple drainage model in map view (a) and cross-section (b). The shaded areas represent water-swept regions. This model predicts that the GWC moves 700 m westward and 90 m updip.

Impedance change comparison

The results of both methods exhibit localized impedance decreases in the reservoir, such as areas A and A' in the updip northwestern part region of the compartment (Figure 11). This can possibly be caused the expansion of gas due to pressure reduction. However, the impedance decrease of the fluid must be large enough to offset impedance increase of the rock frame caused by compaction and frame stiffening, also due to pressure reduction.

Some time-lapse changes are different in the two methods, such as region B and B' around well A2 (Figure 11). Region B shows impedance reduction south and east of the producing well and impedance increase west of the well. In contrast, region B' shows impedance reduction northwest of the well and impedance increase southeast of the well. At the well itself, both methods show minimal change. Reservoir simulations show little saturation change at this location and Gassmann fluid substitution shows that the pressure and saturation change cause minimal impedance change (Appendix A).

Wtihin the area between the original and 2000 GWC, impedance increases similar amounts in both methods except for areas C and C'. Area C exhibits impedance reduction. This area overlaps area C', which shows large magnitude impedance increase. Impedance reduction in area C is not likely; we interpret this area to be water-swept and the GWC to be further westward of area C in 2000. At the end of 2000, well A2 experiences water breakthrough.

Impedance map patterns

The base impedance maps have a smooth distribution of low impedance in the

reservoir area, indicating that fluid phases are homogeneously distributed throughout the pore spaces due to equilibrium over geologic time (Gassmann, 1951 and Wang, 2001). In contrast, the monitor impedance maps show overall impedance increase and patchy low impedance patterns in the original reservoir area. Ideal time-lapse results would be a clear movement of the GWC in the updip direction (west) with a drastic impedance increase in the swept area between the original and mid-2000 GWC. The overall impedance increase in the original reservoir area is due to production of gas and condensate and the replacement by water in the pore space. However, the impedance does not increase to be as high as that of the adjacent aquifer because one fluid never completely replaces another and residual gas saturations have a large impact on keeping impedance low.

The patchy low impedance pattern indicates patchy fluid saturations. Production disturbs the equilibrium distribution of fluid phases and the return to equilibrium may require time periods longer than those between the acquisition of seismic surveys used in time-lapse analysis (Smith et al., 2003), in this case 4.5 years. Smith et al. (2003) demonstrate that in a gas-brine system the effects of nonhomogeneous saturations on velocity are greatest for high-porosity sands and low gas saturations (Sw ≈ 0.80), which are the conditions that we have for the G_M at the time of the monitor survey.

Comparison of Methods

We compare the results of the two methods at well 1 where we have impedance from wireline logs (Figure 14). At the first order, both methods have created a 1990 psuedo impedance log that is similar to the measured pre-production impedance log. The impedance log has a 0.5 ft sample interval and the inverted impedance has a 4 ms sample

interval. Thus, we compare the misfit between the minimum inverted impedance and the average impedance of the GM. The 1990-4DAI trace has a -3 % misfit (397 g/cc ft/s lower); the minimum impedance of the 1990-VAI trace has a 5 % misfit (715 g/cc ft/s higher).

Both methods show impedance increase between the base and monitor inversions. The four inversions use the same Earth Model trend created from the interpolation of the pre-production logs. Additionally, since the inversion of 2000-4D does not incorporate any fluid substitution in the wavelet, the resulting 2000-4DAI is free of any drainage assumptions. At the location of well 1, the 2000-4DAI trace shows an impedance increase of 1868 g/cc ft/s relative to the 1990-4DAI trace (Figure 14a). The 2000-VAI shows an impedance increase of 1252 relative the 1990-VAI trace (Figure 14b).

The method that we present for the time-lapse inversion of non-normalized data sets includes fluid substitution to help scale the wavelet amplitude for the inversion of the monitor survey. Inversion using the multi-well wavelet without fluid substitution at any of the wells (Figure 5e) yields a 2000-VAI minimum impedance of 13843 g/cc ft/s at the location of well 1. Using the multi-well wavelet with fluid substitution at well 1 (Figure 5f) yields a 2000-VAI minimum impedance of 14229 g/cc ft/s (Figure 14b).

The incorporation of fluid substitution in the workflow does not yield circular results. This is because each inversion uses the same multi-well wavelet ate every trace, and this wavelet does not contain any spatial information. Additionally, since the multi-well wavelet is the best-fit to information at several wells, assumptions made at particular locations do not remain.

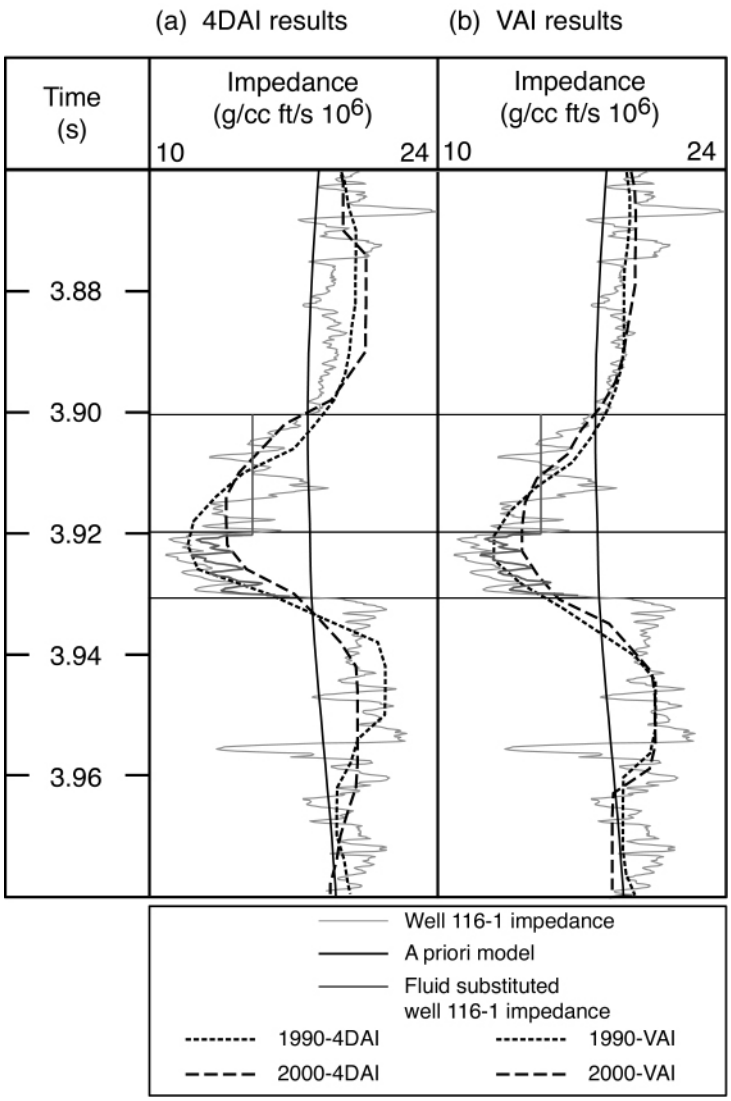

Fig. 14: Comparison of inverted impedance traces near well 1 from both methods with the measured well impedance and fluid-substituted well impedance. Every 0.5 ft sample of the well impedances is displayed; the sample interval of the inverted impedances is 4 ms. The contribution of the Earth Model is only 0-6 Hz.

CONCLUSIONS

The similarity of the inverted impedance results from the two time-lapse inversion methods that we perform indicates that time-lapse processing is not a prerequisite for time-lapse inversion. The time-lapse seismic processing that was applied to normalize the data prior to inversion was successful at removing differences in amplitude and phase. We have shown that these differences can be accounted for by the inversion procedure itself, with the use of wavelets that have been derived for each data set.

As a result, the success of this time-lapse inversion method without prior seismic processing depends on the wavelet. We advocate wavelet derivation procedures that estimate both amplitude and phase, and estimate the entire wavelet (i.e. do not force symmetry). Fluid substitution should be performed to help scale single-well wavelets if the logs were not acquired at the same reservoir conditions as the seismic data. Since the multi-well wavelet used in each inversion does not contain spatial information and is used at every trace, the inverted impedance results do not retain drainage assumptions made at individual well locations.

Application of these two time-lapse inversion methods allows us to image water sweep in the RM compartment of the G-sand due to production. The G-sand experiences overall impedance increase in water-swept regions, but does not increase to aquifer impedance values due to the large acoustic impact of residual gas saturations. The magnitude that impedance increases (884 g/cc ft/s, 6%) is comparable to forward modeling with Gassmann fluid substitution (1079 g/cc ft/s, 8%). In the inverted impedance data, we image the GWC to have migrated up to 900 m westwards and 100 m

vertically upwards; this result is comparable to the 700 m lateral and 90 m vertical movement predicted by a volumetric drainage model. The broad distribution of impedance change and patchy pattern in monitor impedance maps and cross-sections indicates patchy fluid saturations at the monitor time.

REFERENCES

Abubakar, A., van den Berg, P.M., and Fokkema, J.B., 2001, A feasibility study on nonlinear inversion of time-lapse seismic data: SEG International Exposition and Annual Meeting Abstracts.

Debeye, H.W.J. and van Riel, P., 1990, Lp-norm deconvolution: Geophyical Prospecting, **38**, 381-404.

Dennis, L.P., Peterson, F.M, and Todorov, T.I., 2000, Inversion–the importance of low frequency phase alignment: SEG 2000 Expanded Abstracts.

Gassmann, F., 1951, Uber die Elastiziat Poroser Medien: Vier. Der Natur. Gesellschaft in Zurich, **96**, 1-23.

Ghosh, S.K., 2000, Limitations on impedance inversion of band-limited reflection data: Geophysics, **65**, 951-957.

Gluck, S., Juve, E., and Lafet, Y., 1997, High-resolution impedance layering through 3-D stratigraphic inversion of poststack seismic data: The Leading Edge, 1309-1315.

Gluck, S., Deschiezeaux, B., Mignot, A., Pinson, C., and Huguet, F., 2000, Time-lapse impedance inversion of post-stack seismic data: SEG 2000 Expanded Abstracts.

Kojo, Z., Mackowski, T., and Kwasny, G., 1998, Influence of wavelet estimation parameters on inversion of seismic reflection data: Technika Poszukiwan Geologicznych, **37**, 49-57.

Latimer, R.B., Davison, R., van Riel, P., 2000, An interpreter's guide to understanding and working with seismic-derived acoustic impedance data: The Leading Edge, 242-256.

Malinverno, A., 1995, Inversion of seismic and well log data by best feasible approximation: SEG 65th International Meeting, 1032-1146.

Madiba, G.B. and McMechan, G.A., 2003, Seismic impedance inversion and interpretation of a gas carbonate reservoir in the Alberta Foothills, western Canada: Geophysics, **68**, 1460-1469.

Mesdag, P., Van Eykenhof, R., Harmony, B., Harvidaya, L., Sams, M., and Van Riel, P., 2003, Integrated AVO Reservoir Characterization and Time-Lapse Analysis of the Widuri Field: EAGE 65th Conference and Exhibition.

Pendrel, J. and van Riel, P., 1997, Methodology for seismic inversion: a Western Canadian reef example: CSEG Recorder, 22.

Pendrel, J. and van Riel, P., 2000, Effect of well control on constrained sparse spike seismic inversion: CSEG Recorder.

Sakhnovich, L., 1997, Interpolation theory and its applications: Kluwer Academic Publishers.

Smith, T.M., Sondergeld, C.H., and Rai, C.S., 2003, Gassman fluid substitutions: a tutorial: Geophysics, **68**, 430-440.

Swanston, A.M., Flemings, P.B., Comisky, J.T., and Best, K.D., 2003, Time-lapse imaging at Bullwinkle field, Green Canyon 65, offshore Gulf of Mexico: Geophysics, **68**, 1470-1484.

Tennebo, P.O., Veire, H.H., Sonneland, L., Signer, C., and Reymond, B., 1998, Inversion of 4D seismic with best feasible approximation: SEG Expanded Abstracts.

van den Berg, P.M., Broekhoven, A.L., and Abubakar, A., 1999, Extended contrast source inversion: Inverse Problems, 15, 1325-1344.

Walden, A.T. and Hosken, J.W., 1986, The Nature of the non-Gaussianity of primary reflection coefficients and its significance for deconvolution, Geophysical Prospecting, **34**, 1038-1066.

Wang, A., 2001, Fundamentals of seismic rock physics: Geophysics, **66**, 398-412.

White, R.E., 1980, Partial coherence matching of synthetic seismograms with seismic traces: Geophysical Prospecting, **28**, 333-358.

Yuvancic-Strickland, B., Kuhl, E., Lee, T., Seldon, B., Flemings, P.B., and Ertekin, T., 2003, Integration of geologic model and reservoir simulation, Popeye field, Green Canyon 116: GCAGS/GCSSEPM Transactions, **53**, 918-932.

Table 1. Variable definitions.

Variable	Description
A_{obs}	Observed seismic trace
A_{syn}	Synthetic seismic trace from convolution of a *w* with r_z
F	Inversion objective function, total misfit
r_A	Reflectivity from deconvolution of seismic data with a wavelet
r_z	Reflectivity derived from impedance trace
w	Multi-well wavelet
$Z_{trend,model}$	Low-frequency *a priori* model
$Z_{trend,inv}$	Low-frequency trend of inverted impedance
λ	Scaling factor

Table 2. Data set abbreviations.

Name	Description
1990-V	Original base data set 1990 grid system (12.5 m x 20 m)
2000-V	Original monitor data set 2000 grid system (12.5 m x 20 m)
1990-4D	Time-lapse processed base data set 1990 grid system with every other inline (25 m x 20 m)
2000-4D	Time-lapse processed monitor data set 1990 grid system with every other inline (25 m x 20 m)
1990-VAI	Output acoustic impedance from 1990-V inversion 1990 grid system (12.5 m x 20 m)
2000-VAI	Output acoustic impedance from 2000-V inversion 1990 grid system (12.5 m x 20 m)
1990-4DAI	Output acoustic impedance from 1990-4D inversion 1990 grid system with every other inline (25 m x 20 m)
2000-4DAI	Output acoustic impedance from 2000-4D inversion 1990 grid system with every other inline (25 m x 20 m)

Table 3. Acquisition summary of the 1990-V and 2000-V surveys.

Parameter	**1990-V**	**2000-V**
Orientation	90°	90°
Natural bin dimension	12.5 m inline, 40 m crossline	12.5 m inline, 40 m crossline
Maximum offset	4000 m	7200 m
Nominal offset	100	150
Streamers	2	4
Channels/cable	160	288
Source point interval	25 m	37.5 m
Group interval	25 m	25 m
Fold	40	48
Record length	8 s	13 s
Sampling interval	4 ms	4 ms

Table 4. Processing summary of the 1990-V and 2000-V surveys.

1990-V	**2000-V**
Navigation merge	Navigation merge
Designature	Resample from 2 to 4 ms with anti-alias filter
Amplitude recovery / trace editing	Spherical divergence correction
Deconvolution (spiking 320 ms operator)	Minimum phase conversion using modeled far field signature
3D binning	Deconvolution
3D DMO velocity analysis	Radon multiple attenuation
NMO	3D Kirchhoff Bin centering DMO
3D DMO	3D V(z) pre-stack time migration using Stolt algorithm
3D stack (12.5 x 40 m bins)	0.8 km grid final velocity analysis
Crossline interpolation (12.5 x 20 m bins)	Full offset stack
Two-pass migration	Post stack demigration
Bandpass filter / final scaling	Crossline FX trace interpolation
	Zhimming Li steep dip one pass 3D time migration

Table 5. Time-lapse processing summary of the 1990-4D and 2000-4D surveys.

Processs
Regrid 2000-V to 1990-V system
Base and monitor multiple removal
Base and monitor depulse
Base velocity analysis
Monitor global match filter and time-varying gain to match base
Base and monitor 4D static corrections
Base and monitor DMO
Base and monitor noise suppression filter
In-line pre-stack time migration
Monitor filter to match signal spectra of base
Monitor filter to match phase of base
Base and monitor trim filter (trace-by-trace filter with moving overlapping windows)
Monitor time shift to match base
Base and monitor shallow blanking
Time-varying gain function
Base and monitor bandpass filter

Table 6. Inversion Workflow of a Single Seismic Data set.

Step	**Procedure**
1	Interpret horizons and faults on seismic data
2	Edit log data and perform fluid substitution where necessary
3	Well-to-seismic tie and wavelet estimation at each well with select traces
4	Multi-well wavelet estimation
5	Build and populate *a priori* model
6	Set constraints and parameters and invert traces from step 3 for quality control
7	Constrained sparse spike inversion on data of interest

Table 7. Stratigraphic framework for 1990-V.

Interface #	Interface horizon	Stratigraphy between interface above and below
6	Water bottom	
		Proportional to top and base
5	Shallow horizon at 2500 ms	
		Proportional to top and base
4	Horizon above G-sand	
		Parallel to base
3	Base of G-sand	
		Proportional to top and base
2	Horizon below G-sand	
		Proportional to top and base
1	Minibasin base	
		Parallel to top
	End of data—5 s	

Table 8. Summary of change of G-sand minimum impedance.

Method	Aquifer (down-dip of OGWC)			
	Median (g/cc ft/s)	**σ (g/cc ft/s)**	**N**	**Relative (%)**
2000-4DAI - 1990-4DAI	-113	363	3330	-0.74
2000-VAI - 1990-VAI (in 4DAI area)	114	450	6284	0.79
2000-VAI - 1990-VAI	-22	427	12806	< -0.01

Method	Reservoir (up-dip of OGWC)			
	Median (g/cc ft/s)	**σ (g/cc ft/s)**	**N**	**Relative (%)**
2000-4DAI - 1990-4DAI	625	815	3257	5.80
2000-VAI - 1990-VAI (in 4DAI area)	884	1067	6132	6.35
2000-VAI - 1990-VAI	690	1003	13033	6.26

APPENDIX A—GASSMANN FLUID SUBSTITUTION MODELING

INTRODUCTION

We use Gassmann fluid substitution modeling to relate time-lapse results to changes in acoustic properties of the G-sand. Fluid saturation and pressure changes induced by production of hydrocarbons can have a significant effect on the acoustic properties of unconsolidated sand reservoirs (Domenico, 1977).

Gassmann's equation (1951) relates the bulk p-wave modulus of a fluid-saturated rock to its porosity and the bulk moduli of the mineral matrix, fluid, and dry rock. We first determine for the dry rock bulk modulus for the in-situ pre-production scenario when all the other above parameters are known (Zhu et al., 1990). We can then predict the bulk p-wave modulus of the saturated rock as a function of any pressure and pore fluid. The new compressional velocity of the fluid substituted rock is then calculated from the new bulk p-wave modulus and the new density of the saturated rock. We incorporate the effect of pressure changes on porosity, dry bulk modulus, and pore fluid properties (including the condensation of gas), so that the fluid substitution model is comprehensive.

The lithological differences of the two G-sand facies require that they be modeled separately, as they have different model inputs of pressure and fluid saturations at the same lateral position because of different drainage behaviors. Application of Gassmann modeling is straight-forward for the G_M because it is a clean massive sand that meets the model assumptions summarized by Wang (2001). However, Gassmann's equations often produce unreliable results when applied to shaley sands because the basic assumptions

are not valid (Smith et al., 2003). The G_L violates the assumptions that the rock is homogeneous and isotropic and that the pores are interconnected and communicating.

We model the G_L using a laminar mode of mixing where the large grains and small grains fill space separately as alternating laminae of shale and sand on a scale much less than the seismic wavelength. A net-to-gross thickness value is used to separate sands and silty shales. The sand portion of the G_L is fluid substituted; we assume that no changes occur in the silty shales. The porosity of the sand portion is calibrated by core samples. The effective bulk density of the G_L is calculated as the volumetrically-weighted average of shale density and fluid-substituted sand density. The effective compressional velocity is calculated using the Backus average of shale velocity and fluid-substituted sand velocity (Mavko et al., 1998). We model the effective acoustic properties of the G_L as one unit, rather than at each sample of the well logs or for each sand and shale layer.

We generalize the behavior of the G-sand through production with three regions: the aquifer below the original GWC that experiences only pressure depletion, a region swept by water as the GWC moves updip, experiencing reductions in pressure and gas saturation, and areas above GWCs that only experience pressure depletion. Four well locations, in the three regions of the reservoir conditions, are modeled at pre-production and 2000 conditions (Figure A-1). The water-saturated well 2ST1 represents aquifer regions. Water-swept regions are modeled with well 2, where both the G_M and G_L facies are downdip of the 2000 GWC, and at well 1, where the G_M facies is water-swept and the G_L facies remains gas-saturated. Well A2 does not experience water-sweep in either facies, and we use it to understand the regions above the 2000 GWC. The wells are

modeled with initial fluid and pressure conditions and then with fluid-substituted conditions.

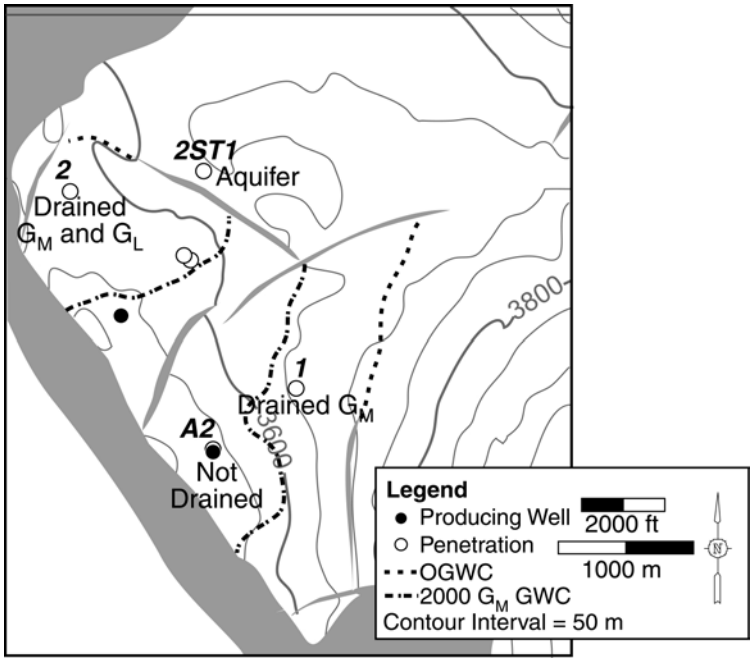

Figure A-1: Wells modeled with Gassmann fluid substitution represent three regions of G-sand with initial and 2000 GWCs in the G_M facies. Well 2ST1 represents the G-sand aquifer, wells 1 and 2 characterize water swept regions, and well A2 represents undrained reservoir regions.

THE EFFECTS OF AQUIFER PRESSURE DEPLETION: WELL 2ST1

We model the effects of pressure reduction within the aquifer using the rock properties from well 2ST1, which is 100 % water saturated. The pressure reduction causes the water density to slightly decrease and become more compressible. However, sand within the facies compacts and stiffens with the pressure drop, which has a greater effect on the bulk G-sand properties. The net effect of pressure decrease at the 2ST1 well is an increase in density, velocity, and impedance. Figure A-2 shows the results of lowering aquifer pressure from 8000 to 5000 psi in the G_M and G_L facies. Both facies

experience increases in density and velocity with decreasing pressure, which causes the impedance of the facies to increase.

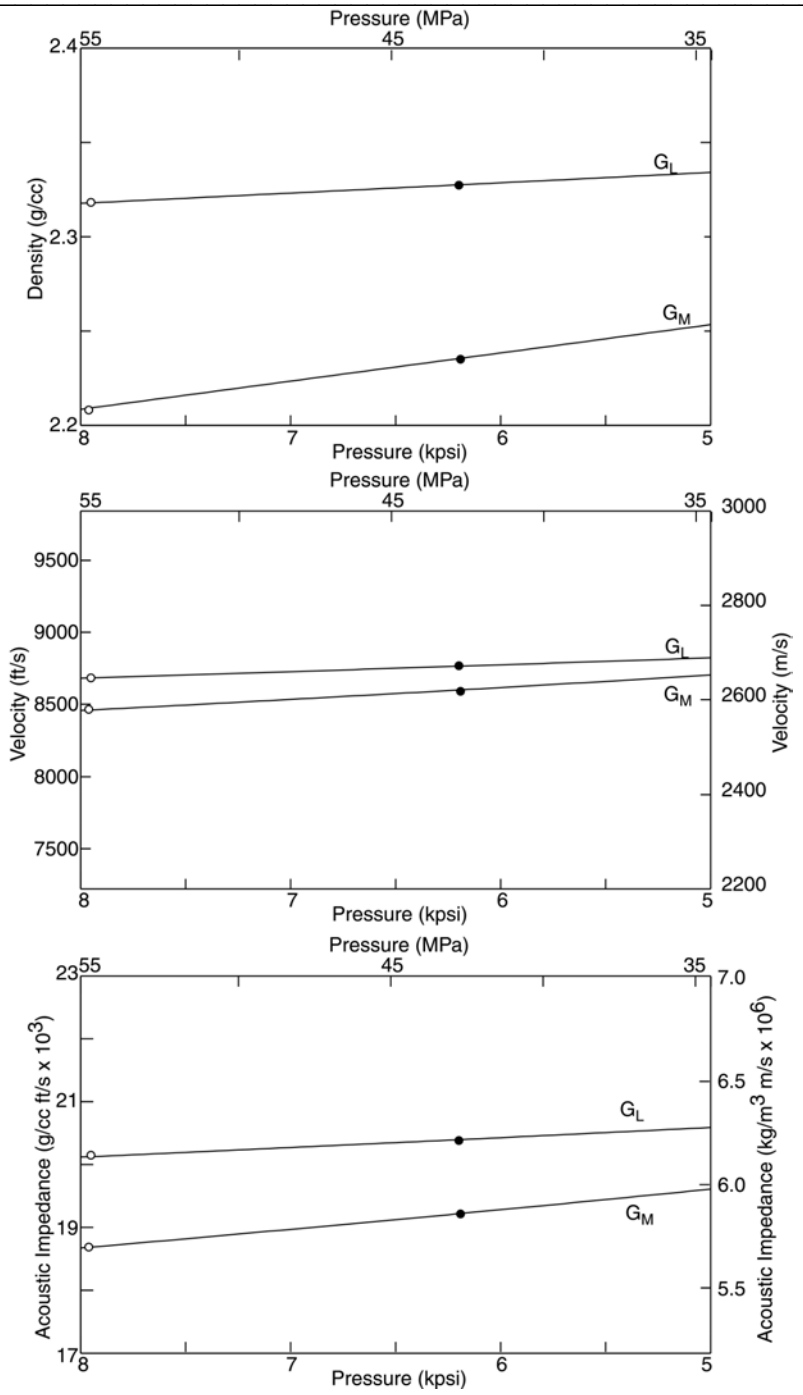

Figure A-2: As pressure decreases in well 2ST1, density, velocity, and impedance all increase due to compaction and frame stiffening. There are minimal fluid effects since the well is water saturated at all times and water has low compressibility. Pre-production density, velocity and impedance are marked with white circles, 2000 density, velocity are indicated with black circles.

Between 1996 and 2000, pressure within the G_M at well 2ST1 decreases from 7961 to 6191 psi and from 7951 to 6199 psi in the G_L facies. This change causes an 8.8 % increase of the G_M impedance, as velocity increases by 187 m/s and density increases 0.031 g/cc (Table A-1). The bulk G_L impedance increases 2.1 % due to the 103 m/s increase in velocity and the 0.024 g/cc increase in density within the G_L sand (Table A-1, Figure A-3). The RFCs of the G-sand are low magnitude because the sand is water-saturated (Figure A-3).

Table A-1: Reservoir properties at well 2ST1.

Parameter		G_M		G_L			
		Initial	2000	Initial		2000	
Stress	P_p (psi)	7961	6191	7951		6199	
Fluid	S_w	1	1	1		1	
	S_g	0	0	0		0	
	S_o	0	0	0		0	
	ρ_f (g/cc)	1.128	1.124	1.128		1.124	
	K_f (MPa)	3356	3335	3356		3335	
Matrix	ρ_m (g/cc)	2.650		2.650			
	K_m (MPa)	38,000		38,000			
Skeleton	K_{dry} (MPa)	4239	4485	1389		1482	
	μ	0.195		0.195			
	ϕ (%)	29.1	27.3	25.0		23.4	
	c_p (psi^{-1})	49.464 x10^{-6}		49.464 x10^{-6}			
Bulk	M (GPa)	16.25	17.107	12.100		13.345	
				Sand	Bulk	Sand	Bulk
	ρ_b (g/cc)	2.202	2.233	2.269	2.318	2.293	2.327
	V_p (m/s)	2579	2766	2309	2626	2412	2670
	Z ($kg/m^3 \cdot m/s$ x10^6)	5.679	6.178	5.240	6.086	5.532	6.214
	Net-to-gross ratio	1		0.4			
Shale	ρ_{sh} (g/cc)	2.350					
	V_{sh} (m/s)	2903					
	Z_{sh} ($kg/m^3 \cdot m/s$ x10^6)	6.822					

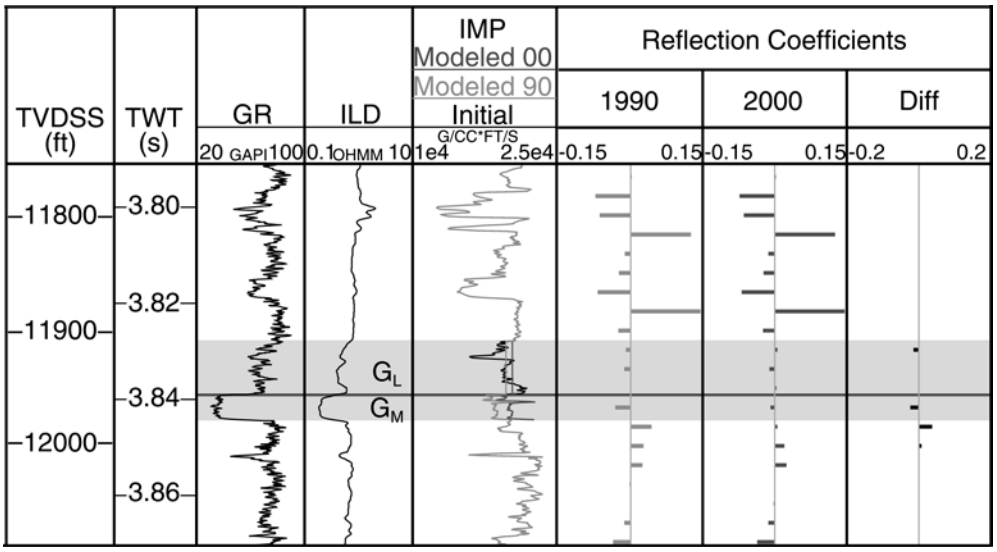

Figure A-3: Well 2ST1 gamma ray (GR), resistivity (ILD), and impedance (IMP) logs in the depth domain and reflection coefficients in the time domain. The G_L facies is modeled as the effective acoustic impedance; these averaged values are used to derive RFCs. The water-saturated nature of the G-sand at well 2ST1 causes low-valued RFCs, differences between 1990 and 2000 RFCs are also small at the G-sand interval

EFFECTS OF WATER SWEEP

G_M Facies—Well 1

We model the effects of reducing the gas saturation (91 % to 23 %) and the pressure (7980 to 6391 psi) in the G_M facies, while maintaining initial gas saturation (68 %) and reducing the pressure (7970 to 6227 psi) within the G_L facies (Table A-2). Initial pressure and saturation values were measured at the well. Pressure and G_M gas saturation for the year 2000 are based on reservoir simulation results; we maintain initial G_L gas saturation in the 2000 fluid substitution to force an impedance decrease. The pressure reduction within the G_M facies causes compaction and stiffening of the rock frame; these effects are not accounted for within the G_L facies. Only the effect of pressure reduction

on fluid properties is modeled in the G_L facies. Even when saturation is held constant, changes in the elastic properties of the saturating fluid, due to pressure changes, affect the acoustic velocity of the rock (Clark, 1992; Alberty, 1996; Jones et al., 1998).

A generalized model for the G-sand as saturation and pressure are varied shows that most of the velocity and impedance change occurs between gas saturations of 0 to 0.15 (Figure A-4). Between gas saturations of 0.15 to 1.0, velocity does not change much (Domenico, 1976) and changes in impedance are largely driven by density changes. In fact, as gas saturations decrease from 1.0, compressional velocity decreases slightly first before it increases. This is because initially density increases at a greater rate than the effect of compressibility reduction; then they switch and velocity increases. This model also shows that lower net-to-gross thickness ratios result in smaller amounts of impedance change as saturation is varied and higher overall impedance (Figure A-5). This is because there is less sand to fluid-substitute and have less effect on the overall bulk rock properties.

The 68 % saturation decrease and 20 % pressure reduction within the G_M facies cause a bulk density increase of 0.113 g/cc and a velocity increase of 61 m/s (Table A-2). Reducing the pressure 22 % within the G_L facies caused a decrease of 0.003 g/cc in bulk density and a decrease of 48 m/s in velocity (Table A-2). The pressure and fluid saturation changes increase the acoustic impedance of the massive facies and decrease the impedance of the laminated facies (Table A-2). Both G_M and G_L layers experience low magnitude changes in acoustic impedance because seismic velocities remain relatively low through a wide range of gas saturations (Figure A-5). When compaction is accounted for in the G_L facies, impedance increases between initial and 2000 conditions.

Table A-2: Reservoir properties at well 1.

Parameter		G_M		G_L			
		Initial	2000	Initial		2000	
Stress	P_p (psi)	7980	6391	7970		6227	
Fluid	S_w	0.09	0.76	0.32		0.31	
	S_g	0.91	0.23	0.68		0.68	
	S_o	0	0.01	0		0.01	
	ρ_f (g/cc)	0.356	0.921	0.551		0.525	
	K_f (MPa)	190	487	249		176	
Matrix	ρ_m (g/cc)	2.650		2.650			
	K_m (MPa)	38,000		38,000			
Skeleton	K_{dry} (MPa)	3094	3251	3480		3480	
	μ	0.195		0.195			
	ϕ (%)	33.0	31.3	30.0		30.0	
	c_p (psi^{-1})	49.464 x10^{-6}		49.464 x10^{-6}			
Bulk	M (GPa)	6.734	7.851	7.572		7.514	
				Sand	Bulk	Sand	Bulk
	ρ_b (g/cc)	1.996	2.109		2.188		2.185
	V_p (m/s)	1865	1926		2153		2105
	Z ($kg/m^3 \cdot m/s$ x10^6)	3.735	4.064		4.711		4.600
	Net-to-gross ratio	1		0.5			
Shale	ρ_{sh} (g/cc)	2.290					
	V_{sh} (m/s)	2438					
	Z_{sh} ($kg/m^3 \cdot m/s$ x10^6)	5.584					

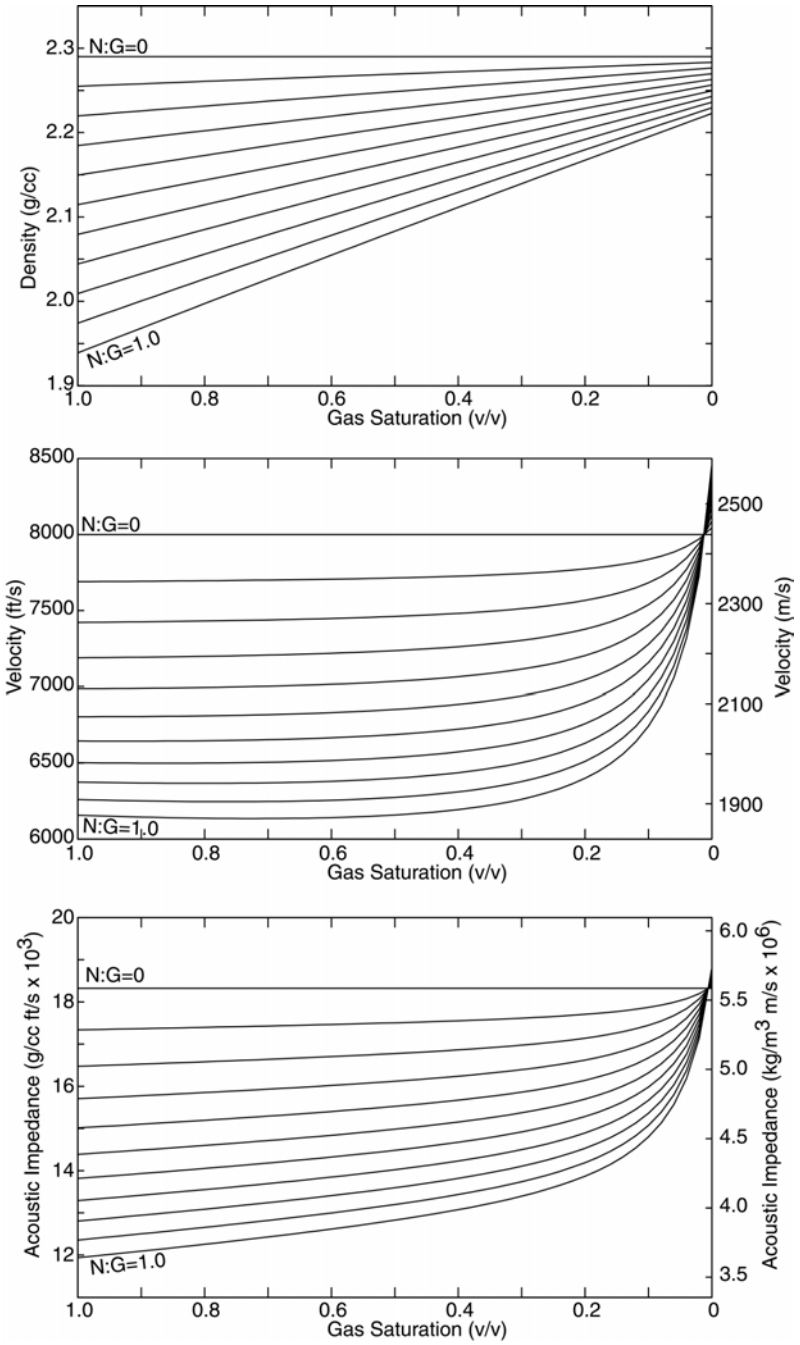

Figure A-4: A generalized acoustic model of the G-sand incorporates pressure reduction from 8000 to 6000 psi and fluid changes from all gas to mostly brine, with oil saturation increasing from 0 to 0.01 and porosity decreasing from 0.30 to 0.28 within the sand. We assume pure shale with no fluid flow (N:G=0), fluid substitute pure sand (N:G=1), and then mix the sand and shale at N:G intervals of 0.1.

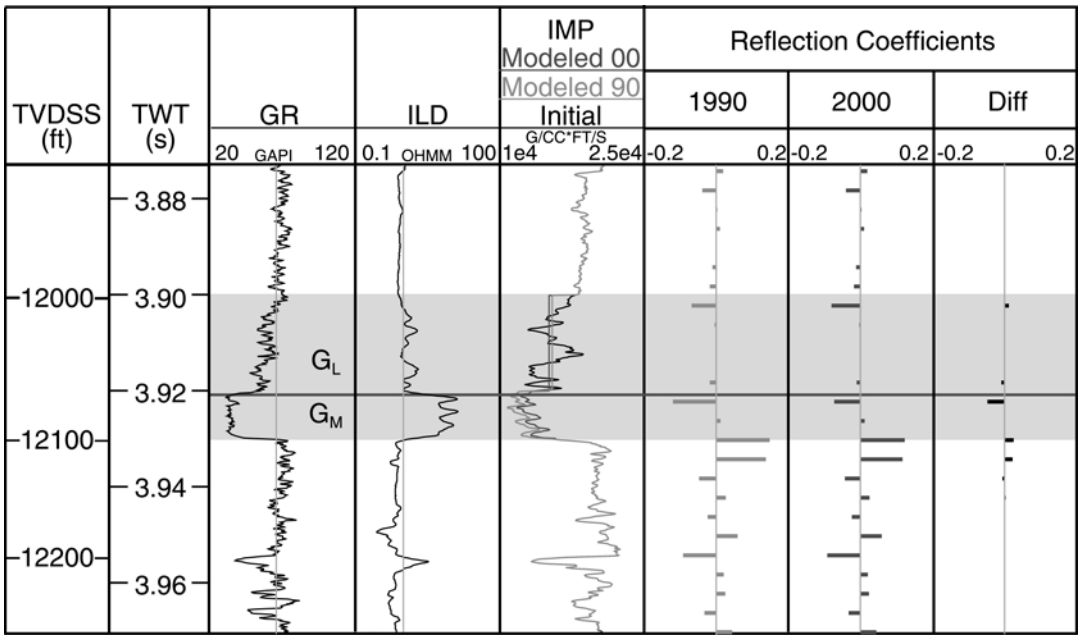

Figure A-5: Well 1 gamma ray (GR), resistivity (ILD), and impedance (IMP) logs in the depth domain and reflection coefficients in the time domain. The G_L facies is modeled as the effective acoustic impedance; these averaged values are used to derive RFCs. The transformation of the impedance log from a sample interval of 0.5 ft in depth to a less frequent sample of 4 ms in time causes band-limiting which smears the reflection response in time. Hence, the time and depth samples do not line up and the G_M base RFCs extend across two time samples.

G_M and G_L Facies—Well 2

The G_M and G_L facies are thin at well 2 (9.4 m total net sand) (Figure A-6), additionally, the net-to-gross ratio of the G_L facies is only 10 % (Table A-3). We interpret that both facies were water-swept by 2000, reducing gas saturation in the G_M facies from 90 to 23 % and from 60 to 23 % in the G_L sand layers (Table A-3). Year 2000 gas saturations are based on residual gas saturations at well 1 within the reservoir simulation. We model that reservoir pressure in the G_M decreased from 7935 to 5302 psi, and the pressure within the G_L decreased from 7924 to 5301 psi, based on initial and

2000 reservoir simulation results. Compaction is accounted for in both facies, which causes reduction of porosity (Table A-3) and stiffening of the rock frame.

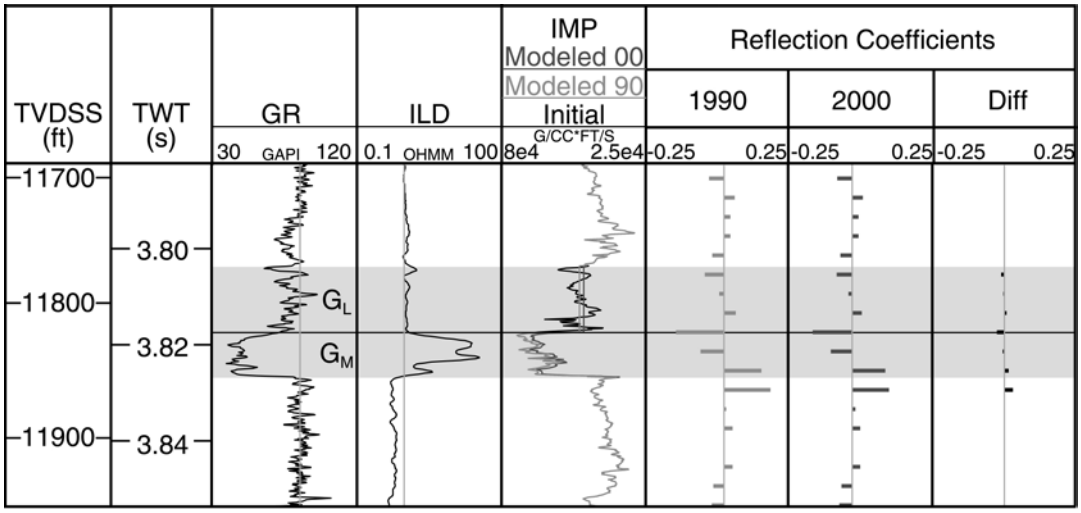

Figure A-6: Well 2 gamma ray (GR), resistivity (ILD), and impedance (IMP) logs in the depth domain and reflection coefficients in the time domain. The impedance values of the G_M and G_L increase between initial and 2000 conditions. The difference between time and depth domains is explained in Figure A-5.

The decrease in reservoir pressure and gas saturation causes velocity and density to increase in both G_M and G_L facies. The impedance of the G_M facies increases 10.8 % while the G_L facies impedance increases only 1.4 % (Table A-6). The small amount of change within the G_L occurs because only 10 % of the unit is affected by water sweep and compaction.

EFFECTS OF GAS EXPANSION IN G_M AND G_L FACIES: WELL A2

Neither facies of the G-sand in well A2 was water-swept by 2000; we model constant gas saturation and diminished reservoir pressure. Figure A-7 shows the effects within the G_M and G_L facies of decreasing reservoir pressure; each facies in the plots of

Figure D are represented with two lines. The dashed line for each facies represents the modeled behavior of density, velocity, and impedance as pressure is reduced, accounting only for changes in fluid properties. As pressure decreases along this trend, density, velocity, and impedance decrease. The solid line of each facies predicts the rock properties as pressure decreases, accounting for fluid property changes and compaction. When compaction effects are incorporated, density, velocity and impedance increase as reservoir pressure decreases (Figure A-7).

Table A-3: Reservoir properties at well 2.

Parameter		G_M		G_L			
		Initial	2000	Initial		2000	
Stress	P_p (psi)	7935	5302	7924		5301	
Fluid	S_w	0.10	0.76	0.40		0.76	
	S_g	0.90	0.23	0.60		0.23	
	S_o	0	0.01	0		0.01	
	ρ_f (g/cc)	0.364	0.910	0.619		0.910	
	K_f (MPa)	191	379	278		379	
Matrix	ρ_m (g/cc)	2.650		2.650			
	K_m (MPa)	38,000		38,000			
Skeleton	K_{dry} (MPa)	3159	3443	3029		3314	
	μ	0.195		0.195			
	ϕ (%)	30.1	27.4	28.0		25.4	
	c_p (psi^{-1})	49.464 x10^{-6}		49.464 x10^{-6}			
Bulk	M	6.924	8.126	6.810		7.910	
				Sand	Bulk	Sand	Bulk
	ρ_b (g/cc)	2.076	2.173	2.081	2.264	2.208	2.281
	V_p (m/s)	1845	1913	1809	2311	1893	2359
	Z ($kg/m^3 \cdot m/s$ x10^6)	3.830	4.161	3.765	5.232	4.179	5.383
	Net-to-gross ratio	1		0.10			
Shale	ρ_{sh} (g/cc)	2.290					
	V_{sh} (m/s)	2438					
	Z_{sh} ($kg/m^3 \cdot m/s$ x10^6)	5.584					

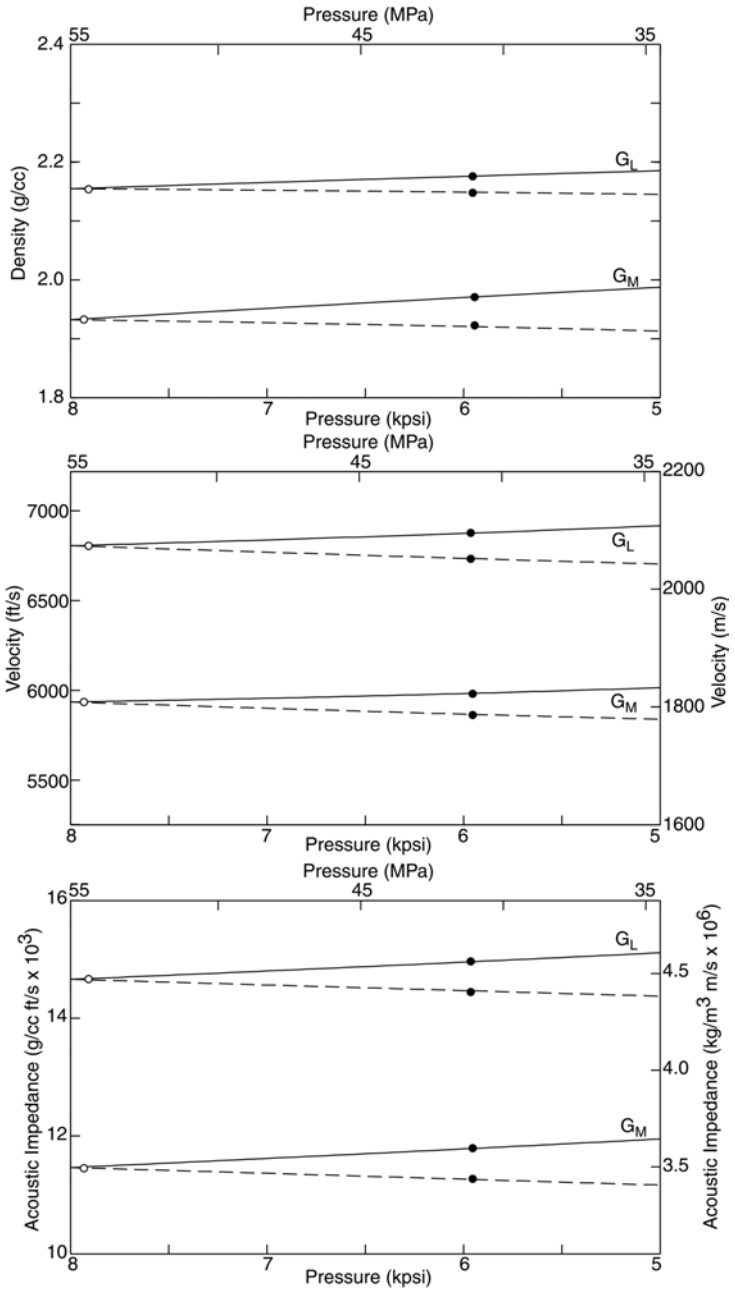

Figure A-7: Effects of pressure reduction on the velocity, density, and impedance of the G_M and G_L facies with pressure reduction at well A2. Density, velocity, and impedance increase with decreasing pressure when changes in fluid properties and compaction are modeled (solid lines). When only fluid property changes are accounted for in the model, density, velocity, and impedance decrease with decreased reservoir pressure (dashed lines). Initial reservoir pressure at well A2 is marked with white circles, 2000 reservoir pressure is indicated with black circles.

At well A2 between 1996 and 2000, reservoir pressure decreases from 7932 to 5954 psi in the G_M facies and from 7908 to 5964 psi in the G_L facies. To force impedance decrease, we model that gas saturation remains constant in both facies (85 %) and that compaction does not affect the sands. If these pressure changes are modeled (allowing gas expansion), impedance decreases by 1.1 % in the G_M facies and by 6.2 % in the G_L facies, if compaction of the sand is not taken into account (Table A-4B, Figure A-8). We also model the difference between initial and 2000 conditions considering the effects of compaction, and that gas saturation in the G_M and G_L facies decreases from 85 to 82 %, based on reservoir simulation results. The impedance of the G_M and G_L facies increases 3.7 and 3.3 %, respectively, when compaction and fluid effects are considered (Table A-4B).

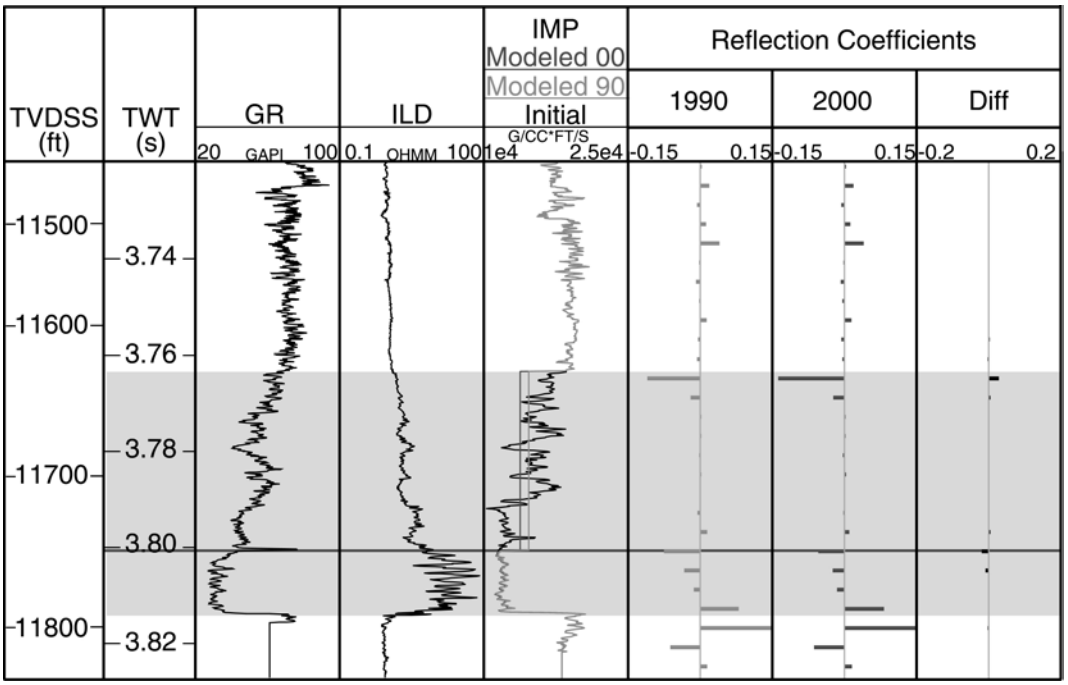

Figure A-8: Well A2 gamma ray (GR), resistivity (ILD), and impedance (IMP) logs in the depth domain and reflection coefficients in the time domain. The impedance values of the G_L decrease between initial and 2000 conditions, GM impedance decreases only 1.1 %. The difference between time and depth domains is explained in Figure A-5.

Table A-4A: Reservoir properties at well A2, saturation constant and no compaction effects.

Parameter		G_M		G_L sand			
		Initial	2000	Initial		2000	
Stress	P_p (psi)	7932	5954	7908		5964	
Fluid	S_w	0.15	0.14	0.15		0.142	
	S_g	0.85	0.85	0.85		0.85	
	S_o	0	0.01	0		0.01	
	ρ_f (g/cc)	0.407	0.371	0.406		0.370	
	K_f (MPa)	201	134	200		133	
Matrix	ρ_m (g/cc)	2.650		2.650			
	K_m (MPa)	38,000		38,000			
Skeleton	K_{dry} (MPa)	2835		2806			
	μ	0.195		0.195			
	ϕ (%)	33.2		27			
	c_p (psi^{-1})	49.464 x10^{-6}		49.464 x10^{-6}			
Bulk	M	6.240	6.075	6.201		6.092	
				Sand	Bulk	Sand	Bulk
	ρ_b (g/cc)	1.902	1.890	2.044	2.154	2.035	2.149
	V_p (m/s)	1808	1787	1742	2071	1730	1955
	Z ($kg/m^3 \cdot m/s$ x10^6)	3.416	3.380	3.560	4.461	3.520	4.201
	Net-to-gross ratio	1		0.60			
Shale	ρ_{sh} (g/cc)	2.320					
	V_{sh} (m/s)	2721					
	Z_{sh} ($kg/m^3 \cdot m/s$ x10^6)	6.314					

Table A-4B: Reservoir properties at well A2, saturation decrease and compaction.

Parameter		G_M		G_L sand			
		Initial	2000	Initial		2000	
Stress	P_p (psi)	7932	5954	7908		5964	
Fluid	S_w	0.15	0.14	0.15		0.142	
	S_g	0.85	0.82	0.85		0.82	
	S_o	0	0.01	0		0.01	
	ρ_f (g/cc)	0.407	0.397	0.406		0.397	
	K_f (MPa)	201	138	200		138	
Matrix	ρ_m (g/cc)	2.650		2.650			
	K_m (MPa)	38,000		38,000			
Skeleton	K_{dry} (MPa)	2.835	3.018	2806		3001	
	μ	0.195		0.195			
	ϕ (%)	33.2	31.2	27.0		25.1	
	c_p (psi^{-1})	49.464 x10^{-6}		49.464 x10^{-6}			
Bulk	M	6.240	6.474	6.201		6.528	
				Sand	Bulk	Sand	Bulk
	ρ_b (g/cc)	1.902	1.948	2.044	2.154	2.084	2.179
	V_p (m/s)	1808	1817	1742	2071	1770	2115
	Z ($kg/m^3 \cdot m/s$ x10^6)	3.416	3.542	3.560	4.461	3.689	4.609
	Net-to-gross ratio	1		0.60			
Shale	ρ_{sh} (g/cc)	2.320					
	V_{sh} (m/s)	2721					
	Z_{sh} ($kg/m^3 \cdot m/s$ x10^6)	6.314					

REFERENCES

Alberty, M., 1996, The influence of the borehole environment upon compressional sonic logs: The Log Analyst, v. 37, p. 30-45.

Clark, V. A., 1992, The effect of oil under in-situ conditions on the seismic properties of rocks: Geophysics, v. 57, p. 894-901.

Domenico, S. N., 1976, Effect of brine-gas mixture on velocity in an unconsolidated sand reservoir: Geophysics, v. 41, p. 882-894.

Domenico, S. N., 1977, Elastic properties of unconsolidated porous sand reservoirs: Geophysics, v. 42, p. 1339-1368.

Gassmann, F., 1951, Elastic waves through a packing of spheres: Geophysics, v. 16, p. 673-685.

Jones, S. M., C. McCann, T. R. Astin, and J. Sothcott, 1998, The effects of pore-fluid salinity on ultrasonic wave propagation in sandstones: Geophysics, v. 63, p. 928-934.

Mavko, G., T. Mukerji, and J. Dvorkin, 1998, The Rock Physics Handbook; Tools for Seismic Analysis in Porous Media: Cambridge, United Kingdom, Cambridge University Press, 329 p.

Smith, T. M., C. H. Sondergeld, and C. S. Rai, 2003, Gassmann fluid substitution: a tutorial: Geophysics, v. 68, p. 430-440.

Wang, Z., 2001, Fundamentals of seismic rock physics: Geophysics, v. 66, p. 398-412.

Zhu, X., G. A. McMechan, and Anonymous, 1990, Direct estimation of the bulk modulus of the frame in a fluid-saturated elastic medium by Biot theory, SEG Abstracts, vol.60: International Meeting and Exposition, Society of Exploration Geophysicists, p. 787-790.

APPENDIX B—INTEGRATION OF GEOLOGIC MODEL AND RESERVOIR SIMULATION, POPEYE FIELD, GREEN CANYON 116

In Pocket